AGU PUBLICATIONS

JGR

Journal of Geophysical Research: Oceans

RESEARCH ARTICLE

10.1002/2016JC011909

Near-bed hydrodynamics and turbulence below a large-scale plunging breaking wave over a mobile barred bed profile

J. van der Zanden[1], D. A. van der A[2], D. Hurther[3], I. Cáceres[4], T. O'Donoghue[2], and J. S. Ribberink[1]

[1]Department of Water Engineering and Management, University of Twente, Netherlands, [2]School of Engineering, University of Aberdeen, UK, [3]Laboratoire des Ecoulements Géophysiques et Industriels LEGI-CNRS, University of Grenoble, France, [4]Laboratori d'Enginyeria Maritima, Universitat Politècnica de Catalunya, Spain

Abstract Detailed measurements are presented of velocities and turbulence under a large-scale regular plunging breaking wave in a wave flume. Measurements were obtained at 12 cross-shore locations around a mobile medium-sand breaker bar. They focused particularly on the dynamics of the wave bottom boundary layer (WBL) and near-bed turbulent kinetic energy (TKE), measured with an Acoustic Concentration and Velocity Profiler (ACVP). The breaking process and outer flow hydrodynamics are in agreement with previous laboratory and field observations of plunging waves, including a strong undertow in the bar trough region. The WBL thickness matches with previous studies at locations offshore from the bar crest, but it increases near the breaking-wave plunge point. This relates possibly to breaking-induced TKE or to the diverging flow at the shoreward slope of the bar. Outer flow TKE is dominated by wave breaking and exhibits strong spatial variation with largest TKE above the breaker bar crest. Below the plunge point, breaking-induced turbulence invades the WBL during both crest and trough half cycle. This results in an increase in the time-averaged TKE in the WBL (with a factor 3) and an increase in peak onshore and offshore near-bed Reynolds stresses (with a factor 2) from shoaling to breaking region. A fraction of locally produced TKE is advected offshore over a distance of a few meters to shoaling locations during the wave trough phase, and travels back onshore during the crest half cycle. The results imply that breaking-induced turbulence, for large-scale conditions, may significantly affect near-bed sediment transport processes.

Key Points:
- Breaking-induced turbulence spreads over the full water column and invades the wave bottom boundary layer
- Reynolds stresses and TKE values in the wave boundary layer increase substantially in the breaking zone
- An increased wave boundary layer thickness is observed in the breaking region along the breaker bar's shoreward slope

Correspondence to:
J. van der Zanden,
j.vanderzanden@utwente.nl

Citation:
van der Zanden, J., D. A. van der A, D. Hurther, I. Cáceres, T. O'Donoghue, and J. S. Ribberink (2016), Near-bed hydrodynamics and turbulence below a large-scale plunging breaking wave over a mobile barred bed profile, *J. Geophys. Res. Oceans*, *121*, 6482–6506, doi:10.1002/2016JC011909.

Received 21 APR 2016
Accepted 30 JUL 2016
Accepted article online 3 AUG 2016
Published online 31 AUG 2016

1. Introduction

Motivated by the need to improve understanding of cross-shore sediment transport processes in the nearshore region, a number of laboratory [e.g., *Ting and Kirby*, 1994, 1995; *Yoon and Cox*, 2010] and field [e.g., *Ruessink*, 2010; *Feddersen*, 2012] studies have addressed the effects of wave breaking on hydrodynamics. Many of these studies focused on the temporal and spatial distribution of breaking-induced turbulence, since turbulent vortices have the potential to entrain and stir sediment particles [*Sumer and Oguz*, 1978]. While wave breaking is highlighted as the dominant source of turbulent kinetic energy (TKE) production in the surf zone [*Thornton and Guza*, 1983; *Ruessink*, 2010; *Yoon and Cox*, 2010], bed-friction-generated turbulence can contribute importantly to turbulence in the lower water column [*Feddersen*, 2012; *Brinkkemper et al.*, 2015].

Turbulence production and transport mechanisms depend on breaker type [*Ting and Kirby*, 1994]. In the case of a plunging breaker (the focus of the present study), turbulent vortices are formed at the wave front [*Kimmoun and Branger*, 2007; *Sumer et al.*, 2013] and a major part of the breaking-induced TKE is dissipated within the turbulent bore above wave trough level [*Svendsen*, 1987; *Govender et al.*, 2002]. The remainder is injected into the water column and is advected shoreward and downward by the plunging jet and large-scale vortices [*Ting and Kirby*, 1995; *Christensen and Deigaard*, 2001; *Melville et al.*, 2002; *Kimmoun and Branger*, 2007]. Turbulent dissipation rates under breaking waves have been found to be depth-uniform [*Grasso et al.*, 2012] or to decrease with depth [*Feddersen and Trowbridge*, 2005; *Yoon and Cox*, 2010], leading to a general reduction of TKE from the water surface downward [e.g., *Ruessink*, 2010]. Despite the dissipation of breaking-induced turbulence over the water column, a fraction may still reach the near-bed region [*Grasso et al.*, 2012]. TKE profiles have been found to vary in the cross-shore direction and depend on the bed topography, with highest TKE found at the breaker bar crest and lower TKE above the bar trough [*Scott et al.*, 2005; *Yoon and Cox*, 2010].

Small-scale experiments revealed strong phase-dependency of TKE under plunging breakers, with highest values during the wave crest phase for a major part of the water column [*Ting and Kirby*, 1995; *Govender et al.*, 2002]. Depending on breaker characteristics and local water depth, this phase-dependency may reverse near the bed [*Boers*, 2005]. It is believed that the phase-dependency of breaking-induced TKE is coherent with near-bed wave-related sediment transport [*Ting and Kirby*, 1994; *Boers*, 2005; *Ting and Nelson*, 2011].

While significant attention has been paid to hydrodynamics in the breaking region, few studies have focused on the wave bottom boundary layer (WBL) under breaking waves. Breaking-induced vortices may invade the WBL [*Cox and Kobayashi*, 2000; *Huang et al.*, 2010; *Chassagneux and Hurther*, 2014] and can substantially enhance near-bed TKE [*Scott et al.*, 2005] and bed shear stresses [*Deigaard et al.*, 1991; *Cox et al.*, 1996; *Sumer et al.*, 2013]. Most of these studies were conducted in small-scale wave flumes (mostly over rigid, planar sloping beds), which may not fully reproduce the properties of breaking-induced turbulence and of the WBL hydrodynamics under full-scale waves. To the authors' knowledge, previous *large-scale* experiments have not produced high-resolution measurements within the WBL across the wave breaking region. Such measurements are important for better understanding of wave breaking effects on sediment transport processes.

This paper studies the hydrodynamics under large-scale, plunging breaking waves above a mobile-sand barred bed profile. The paper particularly addresses how wave nonuniformity and wave breaking affect the near-bed hydrodynamics, including the WBL.

The experimental conditions, details of instrumentation, and data processing procedures are presented in section 2. Measurements of the breaking process and outer flow velocities are presented in section 3. Section 4 presents the time-averaged and phase-averaged near-bed velocities and section 5 presents the spatial and temporal variability of near-bed turbulence. The wave-breaking effects on the WBL hydrodynamics and the implications for sediment transport processes are discussed in section 6.

2. Experiments

2.1. Facility and Test Conditions

The experiments were carried out in the 100 m long, 3 m wide, and 4.5 m deep CIEM wave flume at the Universitat Politècnica de Catalunya (UPC) in Barcelona. The experimental set-up and bed profile are shown in Figure 1. In this figure and throughout the document, the cross-shore coordinate x is defined positively toward the beach with $x = 0$ at the wave paddle. Vertical coordinate z is defined positively upward from the still water level (SWL); ζ is the vertical coordinate from the local bed level upward.

The initial bed configuration (i.e., before the waves developed the barred beach) comprised a 1:10 offshore slope, followed by an 18 m long and 1.35 m high horizontal test section (Figure 1a). The bed profile consisted of sand with median diameter $D_{50} = 0.24$ mm. Shoreward of the test section ($x > 68.0$ m), the profile followed a 1:7.5 slope covered with geotextile and perforated concrete slabs designed to prevent erosion and promote wave energy dissipation. The water depth, h, at the wave paddle was 2.55 m.

Regular (monochromatic) waves were generated with wave period $T = 4.0$ s and wave height $H = 0.85$ m at the wave paddle. The surf similarity parameter is $\xi_0 = 0.54$, where $\xi_0 = \tan(\alpha)/\sqrt{H/L_0}$, α being the 1:10 offshore slope and L_0 the deep-water wave length [*Battjes*, 1974]. The breaking waves were of the plunging type, in agreement with the classification of *Battjes* [1974].

Figure 1b indicates the breaking point ($x = 53.0$ m), the plunge point ($x = 55.5$ m), and the splash point ($x = 58.5$ m). These points were established from measurements and visual observations of the water surface, as described further in section 3.1, and are used to define the shoaling region ($x < 53.0$ m), the breaking region ($53.0 < x < 58.5$ m) and the inner surf zone ($x > 58.5$ m).

2.2. Instrumentation

The primary instrumentation was deployed from a custom-built mobile frame (Figure 2). The frame was constructed from 30 mm diameter stainless-steel tubing and was designed to minimize flow interference while being sufficiently stiff to withstand wave forces. The frame was mounted to a horizontally mobile

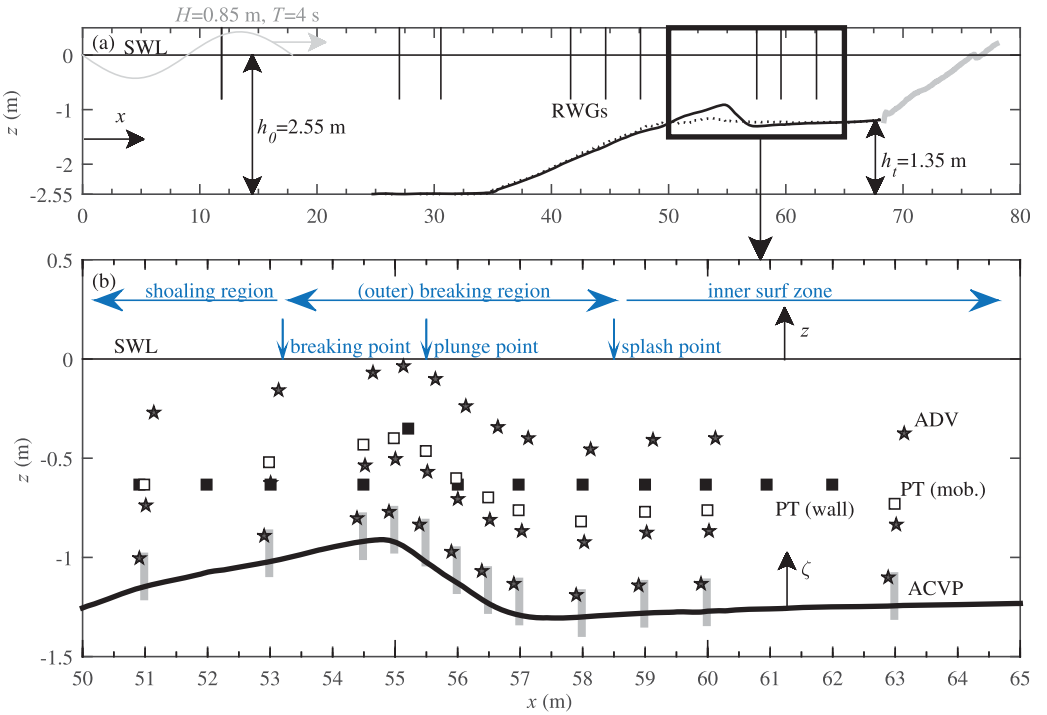

Figure 1. Bed profile and measurement locations. (a) General overview of wave flume, including initial horizontal test section (dotted line), reference bed profile (solid bold black line), fixed beach (solid grey line), and locations of resistive wave gauges (black vertical lines); (b) Close-up of test section, including reference bed profile and instrument positions: mobile-frame pressure transducer (PT mob.; white squares); wall-mounted PTs (black squares); mobile-frame ADVs (stars); and ACVP profiles (grey rectangles).

trolley on top of the flume, and could be vertically positioned with submillimeter accuracy using a spindle. More details of the measurement frame are provided by *Ribberink et al.* [2014].

Outer flow velocities (i.e., higher than 10 cm above the bed) were measured using a vertical array of three Nortek Vectrino acoustic Doppler velocimeters (ADVs, Figure 2). All ADVs operated at an acoustic frequency of 10 MHz and provided three-component (cross-shore, lateral, and vertical, denoted *u*, *v*, and *w*,

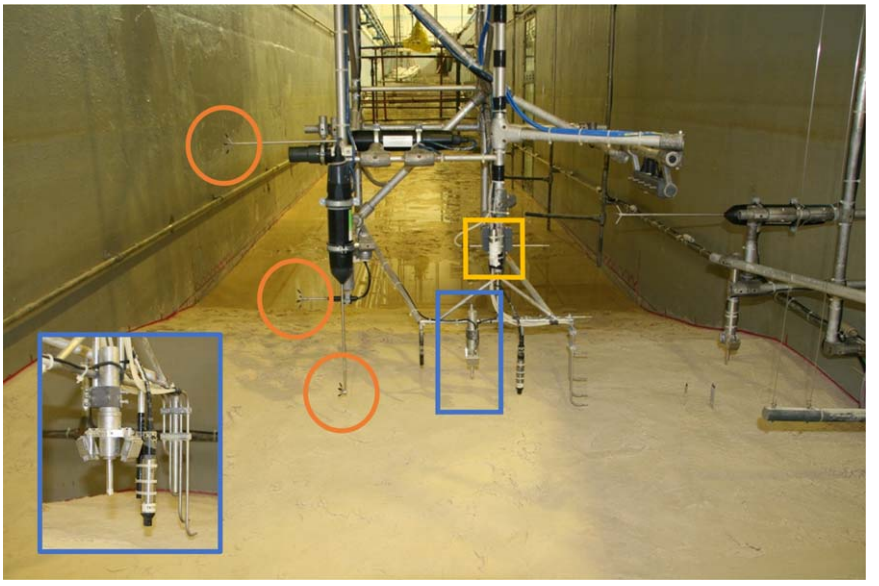

Figure 2. Photo of measuring frame, taken from top of breaker bar while facing the beach. Highlighted instruments: ADVs (orange circles); PT (yellow square); and ACVP (blue rectangle). Inset shows close-up of ACVP.

respectively) velocity measurements at a rate of 100 Hz. The sampling volume is a cylinder-shaped volume with 3 mm radius and 2.8 mm height. The ADVs were located at elevations of approximately 0.11, 0.41, and 0.85 m above the initial (i.e., at start of run) bed.

Near-bed velocities (i.e., below 10 cm above the bed) were measured using a downward-looking High-Resolution Acoustic Concentration and Velocity Profiler (ACVP, Figure 2 inset), described in more detail in *Hurther et al.* [2011]. The ACVP measures simultaneous and colocated vertical profiles of (*u, w*) and sediment mass concentrations [*Hurther et al.*, 2011], hereby providing the possibility to measure intrawave, multidirectional sediment flux. In the present experiment, the ACVP acoustic and geometrical settings were set to measure velocities up to 1.8 m/s over a vertical profile of 20 cm with a vertical bin resolution of 1.5 mm, a horizontal radius of the sampling volume of about 3 mm, and sampling frequency of 70 Hz. Operating at an acoustic frequency of 1 MHz, considerably lower than the frequency of commercial ADV technology, the ACVP enables velocity and concentration measurements to be made within the near-bed sediment layer [cf., *Naqshband et al.*, 2014; *Chassagneux and Hurther*, 2014; *Revil-Baudard et al.*, 2015].

Water surface elevations were measured at 40 Hz using resistive (wire) wave gauges (RWGs) and pressure transducers (PTs) at 21 locations along the flume (Figure 1) and one additional PT attached to the mobile frame (Figure 2). In the breaking region, the horizontal spacing of the measurements was approximately 1 m. In this region, PTs were deployed instead of RWGs because wave splash reduces the data quality of the RWGs. Linear wave theory was used to convert the dynamic pressure measurements (PT) into water surface elevations. Following *Guza and Thornton* [1980], the conversion was applied to frequencies up to 0.33 Hz, which includes the primary wave component (0.25 Hz) but not its higher harmonics. A comparison with RWG-measured water surface elevation in the shoaling zone indicated that the PT-derived wave height underestimates the RWG-measured wave height by up to 10%. The underestimation in higher-order statistics (wave skewness, asymmetry) is more severe.

Bed profile measurements were obtained along two transects, using echo sounders deployed from a second mobile carriage, at a horizontal resolution of 2 cm and with an estimated bed measurement accuracy of $+/-$ 1 cm. The transects were taken at a lateral distance of 0.1 and 0.7 m with respect to the flume's centerline. Bed profiles presented in this paper are based on the average of the two transects.

2.3. Measurement Procedure

To create the reference bed profile for this experiment, regular waves ($H = 0.85$ m, $T = 4$ s) were generated for 105 min over the initial profile described in section 2.1. Subsequently, the flume was slowly drained, bed forms and lateral bed asymmetries were flattened out, and the resulting barred profile was drawn on the flume sidewalls to give the template for the reference bed profile (Figure 1).

Each experiment was run for 90 min of waves, comprising of six 15 min runs, during which the bed further evolved. The bed profile was measured at the start of each experiment and after every second run, i.e., at 0, 30, 60, and 90 min. After the sixth run, the flume was drained and the reference profile was restored by shoveling back the transported sand and flattening out any bed forms that were generated. This sequence of bed profile development and subsequent restoration to the reference profile was repeated 12 times (12 experimental days), where for each experiment the mobile frame was positioned at a different cross-shore location (Figure 1b).

As a reference throughout the paper, Table 1 presents wave height, water depth, velocity, and local bed slope measurements for each mobile-frame measurement location.

2.4. Morphology and Experimental Repeatability

A prerequisite for combining the measurements from different cross-shore locations into one data set is that the experiment is repeatable in terms of wave conditions and bed evolution. Figure 3 shows a comparison of measured bed profiles at different stages of bar development. The good agreement between the profiles confirms the repeatability of the bed evolution. The locations of the smaller bed forms varied with each repeat, but the dimensions and growth rate of the main features of the profile—the breaker bar and trough—were very similar between experiments. The repeatability of bed profile evolution can be quantified by the standard deviation over the 11 profiles at $t = 90$ min, which was 3 cm in the region 50.0 m $< x <$ 67.0 m, including the variability due to smaller bed forms. Wave heights were also similar between

Table 1. Measured Water Level and Velocity Statistics at All Measurement Locations (t = 0–15 Min.)[a]

x (m)	51.0	53.0	54.5	55.0	55.5	56.0	56.5	57.0	58.0	59.0	60.0	63.0
h (m)	1.10	0.97	0.88	0.88	0.97	1.10	1.19	1.24	1.28	1.28	1.26	1.26
β (°)	4	3	2	−6	−13	−11	−10	−4	1	1	2	0
H (m)	0.79	0.74	0.64	0.60	0.51	0.50	0.53	0.48	0.47	0.43	0.42	0.41
$\bar{u}$ (m/s)	−0.13	−0.22	−0.19	−0.24	−0.23	−0.30	−0.51	−0.54	−0.46	−0.36	−0.36	−0.34
u_{on} (m/s)	1.04	0.80	0.84	0.78	0.57	0.25	0.05	0.02	0.01	0.13	0.17	0.19
u_{off} (m/s)	−0.83	−0.94	−0.85	−0.90	−0.83	−0.82	−0.83	−0.78	−0.71	−0.71	−0.66	−0.58
a (m)	0.54	0.48	0.47	0.47	0.39	0.31	0.25	0.23	0.21	0.23	0.24	0.23
$a/k_s/10^3$	2.3	2.0	2.0	2.0	1.6	1.3	1.0	1.0	0.03	0.03	0.03	0.03
$Sk(u)$	0.61	0.44	0.50	0.48	0.36	0.06	0.67	0.95	0.82	0.39	0.67	0.79
$Asy(u)$	0.68	1.01	0.82	0.76	0.75	0.77	0.76	0.58	0.79	0.88	0.68	0.45
$Re/10^5$	5.6	4.5	4.0	4.2	3.3	2.6	2.1	1.8	1.5	1.7	1.6	1.3

[a]Local water depth (h); local bed slope at start experiment (β); wave height (H); time-averaged horizontal velocity ($\bar{u}$); peak onshore and offshore phase-averaged horizontal velocities (u_{on} and u_{off}); semi-excursion length ($a = \sqrt{2}T\tilde{u}_{rms}/2\pi$); Nondimensional semi-excursion length a/k_s, with roughness k_s estimated based on grain size and measured ripple dimensions using formulations by *van der A et al.* [2013]; Velocity skewness ($Sk(u) = \tilde{u}^3/\tilde{u}^3_{rms}$); Velocity asymmetry ($Asy(u) = -\mathcal{H}(\tilde{u})^3/\tilde{u}^3_{rms}$, where $\mathcal{H}$ is the Hilbert transform [e.g., *Ruessink et al.*, 2011]; Reynolds number ($Re = a{\cdot}\tilde{u}_{on}/\nu$; where kinematic viscosity $\nu = 1.0{\cdot}10^{-6}$ m^2/s). Velocity-based variables are based on measurements from the lowest *ADV* ($\zeta = 0.11$ m).

experiments, with a standard deviation (calculated over 12 experimental days) in mean wave height per cross-shore location of less than 2 cm (mean value over all RWGs and PPTs).

During the experiment, the breaker bar increased in height while its trough deepened (Figure 3). The offshore slope before the bar crest gradually increased in steepness, up to a 1:8 steepness after 90 min. The bar growth and steepening induces enhanced shoaling and an increase in ξ_0 (up to 0.68), resulting in an increasing plunging intensity throughout the experiment.

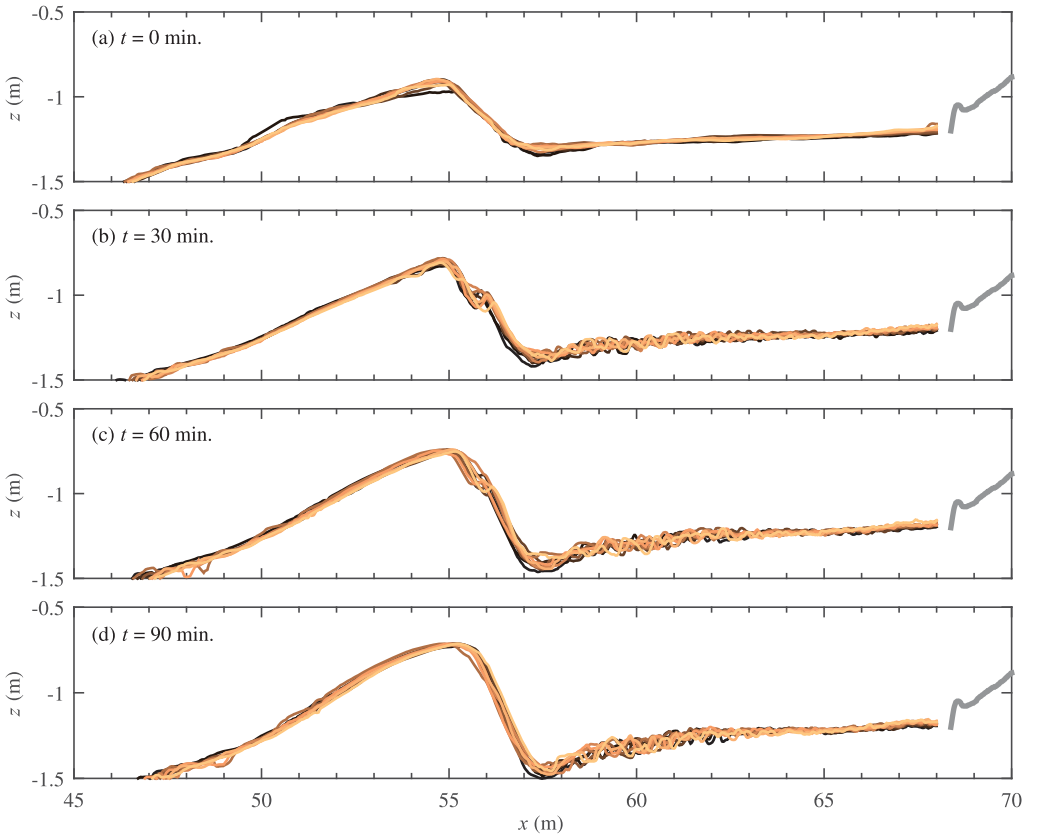

Figure 3. Measured bed profiles for each measurement day. Each plot contains 11 profile measurements, taken at the same stage of profile development (data for one measurement day were discarded due to calibration issues).

Figure 3 indicates the presence of bed forms, starting at the lee (shoreward) side of the breaker bar. Visual observations of the bed after draining the flume confirmed a gradual transition of shoreward-facing lunate-shaped features in the bar trough ($x = 57.0$ to 59.0 m), to quasi-2-D features (with short wave length in wave direction but long wave length in wave-normal direction; $x = 59.0$–62.0 m), to irregular 3-D vortex ripples in the inner surf zone ($x > 62.0$ m). Quasi-2-D bed forms were also observed at the lee side of the bar, where they progressively migrated offshore and upslope (Figure 3b and 3c). At the bar crest, the absence of bed features indicates sediment transport in the sheet flow regime. Further down the offshore slope ($x < 48$ m), a region that is not further considered in the present study, quasi-2-D mega ripples were observed.

2.5. Data Treatment

This paper focuses on measurements obtained during the first run of each measurement day, i.e., for the first 15 min of profile development. Later stages of bar development showed qualitatively similar behavior in terms of hydrodynamic processes; data for these later stages are included in the Reynolds stress results, which were averaged over the entire 90 min experiment in order to minimize the statistical bias error.

Visual observations and water surface measurements showed that the location of wave breaking varied in time during the first 5 min of each run. After this transient phase, the breaking location stabilized, indicating that a hydrodynamic equilibrium was established. Data obtained during the first 5 min of each run were therefore discarded, leaving 10 min of data per run for quantitative analysis. Flume seiching induced a standing wave with an amplitude of O(cm) and a period of about 45 s that matches the natural frequency of the body of water in the flume when $h = 2.55$ m. The standing wave was removed from the velocity and water surface level measurements by applying a high-pass filter with a cut-off frequency of half the primary wave frequency (0.125 Hz).

ADV data were contaminated with noise, predominantly due to high bubble concentrations in the breaking region and with signal dropout when measuring above the water level. ADV data were considered as outliers wen the signal-to-noise ratio was $<$15 dB, or the correlation was $<$50% for time-averaged quantities or $<$80% for instantaneous (turbulent) quantities. The correlation threshold was lower for time-averaged quantities, because the averaging procedure contributes to noise cancellation. Outliers in phase ensembles were identified if the value deviated by more than 3 times the standard deviation from the median at the given phase. Identified outliers were removed from the time series and not substituted by other values. The percentage data points removed varied in the cross-shore direction, from about 10% in the shoaling and inner surf zone, up to 45% in the highly aerated water column under the plunging wave.

For the ACVP measurements, a ζ level was first assigned to each measurement bin based on the measured wave-averaged bed level. The continuous bed level was obtained from the maximum backscatter intensity, following *Hurther and Thorne* [2011]. Horizontal and vertical velocity measurements were transposed to bed-parallel and bed-normal velocities, using a rotation angle that minimized the periodic component of bed-normal velocities close to the bed (at $\zeta = 0.03$ m). This transposition was applied on a wave-by-wave basis. The mean rotation angle obtained with this method at the different cross shore positions was close to the local bed slope estimated from the mechanical bed profile measurements. For simplicity, we refer to the bed-parallel velocities as the "horizontal" velocities and the bed-normal velocities as the "vertical" velocities in what follows.

The phase-averaged value of arbitrary variable ψ is denoted with angle brackets and was calculated from

$$<\psi>(\mathrm{t}) = \frac{1}{N}\sum_{\mathrm{n}=1}^{N}\psi(t+(n-1)T) \tag{1}$$

where N represents the number of wave cycles. N was about 150 for the water surface and outer flow velocity measurements, and somewhat lower for the ACVP measurements (typically about 100, with a minimum of 40). The reason for this difference is that data were discarded when the local bed eroded outside the ACVP maximal profiling range or accreted to distances within the first 5 cm of the ACVP profile. Phase-averaged near-bed velocities (ACVP) were calculated for each ζ bin class with 1.5 mm bin size. To calculate the phase-averaged quantities, reference zero-up crossing of the waves, were obtained from the RWG at

$x = 47.6$ m. Data were then phase-referenced such that $t/T = 0$ corresponds to maximum water surface (wave crest) at the beginning of the test section ($x = 50.0$ m).

The quasi-2-D bed forms observed in the breaking zone had cross-shore wave lengths that were (much) higher than the local orbital amplitude a. Hence, it may be assumed that these bed forms do not induce flow separation and do not contribute to apparent wave-related bed roughness [*van Rijn*, 2007]. The latter is not true for the inner surf zone ($x > 59.0$ m), where bed forms migrated below the ACVP sensors. For these locations, time intervals for phase-averaging of ACVP measurements were chosen such that an integer number of bed forms was captured (i.e., the presented data are averaged over exactly one or multiple ripples) and $\zeta = 0$ corresponds to the time-varying bed interface of the bed form.

Velocities were decomposed into time-averaged ($\bar{u}$, $\bar{w}$), periodic ($\tilde{u}$,$\tilde{w}$), and turbulent (u', w') contributions. Time-averaged quantities are denoted with an overbar and were calculated using

$$\bar{\psi} = \frac{1}{T}\int_0^T <\psi(t)> \mathrm{d}t \tag{2}$$

For the discontinuous velocity measurements above wave trough level, $\tilde{\psi}$ represents the truncated mean based on the "wetted period" instead of the full wave period for T in equation (2). The periodic component is obtained from $\tilde{\psi} = <\psi> - \bar{\psi}$. Root-mean-square magnitudes of $\tilde{\psi}$ are denoted with subscript *rms* and are calculated through:

$$\tilde{\psi}_{\mathrm{rms}} = \left[\frac{1}{T}\int_0^T \tilde{\psi}(t)^2 \mathrm{d}t\right]^{0.5} \tag{3}$$

Various methods exist to extract the turbulent component from the time series [*Svendsen*, 1987; *Scott et al.*, 2005]. The regular waves in the present experiment enable a Reynolds decomposition based on the ensemble-average, i.e., $\psi' = \psi - <\psi>$. Compared to other methods [see e.g., *Scott et al.*, 2005], ensemble-averaging yields the most accurate turbulence estimations since it does not discard contributions of the largest vortices [*Svendsen*, 1987]. However, by adopting this method, wave-to-wave variations due to offsets in phase-referencing and as a result of modulation of velocities and the breaking location by the long wave (flume seiching) may be incorrectly denoted as turbulence [*Svendsen*, 1987; *Scott et al.*, 2005]. These "pseudo-turbulence" contributions are largely suppressed through the aforementioned high-pass filter (0.125 Hz). However, examination of the autospectra of u' and w' revealed that the Reynolds decomposition removes most, but not all, of the energy associated with the wave and its higher harmonics (see Appendix Figure A1). By integrating the autospectra of u' with and without the energy still contained at the first three wave harmonic frequencies (0.25, 0.50, 0.75 Hz), it was found that the time-averaged turbulence intensities are overestimated by approximately 7%. This error cannot be easily removed from turbulent velocity time series. The error is quite small compared to typical spatial and temporal variations of turbulence intensities in this study and is therefore considered acceptable. The effect of wave bias on the Reynolds stresses was separately tested using ogive curves [*Feddersen and Williams*, 2007] and led to the exclusion of nine runs (as detailed in Appendix A).

Phase-averaged *rms* turbulence intensities were calculated through

$$\psi'_{\mathrm{rms}}(t) = \left[\frac{1}{N}\sum_{n=1}^{N}\left(\psi(t+(n-1)T) - <\psi(t)>\right)^2\right]^{0.5} \tag{4}$$

Estimates of $<\psi'_{\mathrm{rms}}>$ are accepted only for $N>40$ to guarantee a low statistical bias error. For the three-component ADV data, the TKE, noted k, can be calculated from the turbulence intensities through

$$<k(t)> = 0.5\left(<u'(t)^2> + <v'(t)^2> + <w'(t)^2>\right) \tag{5}$$

Because of acoustic noise, the ACVP measurements were processed differently. A full explanation of the ACVP data processing is presented in Appendix A. In short, the acoustic noise was largely removed using a despiking routine. Phase-averaged turbulence intensities were then calculated using a two-point cross-

correlation applied to velocities measured at two vertical bin elevations [*Garbini et al.*, 1982; *Hurther and Lemmin*, 2001]. $<k(t)>$ was estimated as $1.39 \cdot 0.5(<u'(t)^2> + <w'(t)^2>)$, where the factor 1.39 is the typical value taken for a turbulent WBL [*Svendsen*, 1987]. Contributions from small-scale high-frequency turbulent fluctuations to turbulence intensities are partly removed using the methodology, leading to an underestimation of TKE and Reynolds shear stress (Appendix A). The underestimation increases toward the bed as the length scale of eddies reduces. Analyses in this study will therefore exclude ACVP turbulence measurements within the lowest 5 mm from the bed. Finally it is noted that in dense suspension layers, the ACVP measures (turbulent) velocities of sand grains that may differ from the fluid velocities (Appendix A).

3. Water Surface Elevation and Outer Flow Velocities

3.1. Surface Elevation

The breaking process is examined by combining phase-averaged RWG and PT measurements of the water surface elevation (Figure 4). On arrival at the test section, the pitched-forward, asymmetric shape of the wave is evident and is caused by wave shoaling along the offshore slope. As the wave propagates toward the bar crest, the wave crest starts to turn over at $x = 53.0$ m (at approximately $t/T = 0.17$). Following *Svendsen et al.* [1978], this location is referred to as the "breaking point." As wave propagation continues, the plunging jet from the breaking wave hits the water surface approximately 2.5 m further at $x = 55.5$ m and at $t/T = 0.33$ ("plunge point," after *Peregrine* [1983]). The jet pushes up a wedge of water and creates a new wave that leads the remainder of the original wave; the remainder of the original wave is called the secondary wave in what follows. This breaking process, including the formation of the secondary wave, is similar to detailed descriptions by *Ting and Kirby* [1995] for a small-scale plunging wave. While propagating further onshore, the water mass pushed up by the plunging wave hits the water surface around $x = 58.5$ m ($t/T = 0.65$). At this "splash point" [*Smith and Kraus*, 1991], the wave reforms into a surface roller with a quasi-uniform shape throughout the remainder of the test section ($x > 58.5$ m). Based on these observations and after *Svendsen et al.* [1978], we distinguish (see Figure 1) the shoaling zone (up to the breaking point at $x = 53.0$ m), the (outer) breaking zone (from breaking point to splash point; $x = 53.0$–58.5 m), and the inner surf zone ($x > 58.5$ m).

The maximum (crest) and minimum (trough) phase-averaged water levels are shown in Figure 5, and can be used to analyze the cross-shore variation of wave height H (see also Table 1). The wave height gradually increases over the offshore slope as a result of wave shoaling (Figure 5a, up to $x = 52$ m). Wave energy dissipation starts near the breaking point at $x = 53$ m and continues through the breaking zone; H is reduced by 50% between $x = 52$ m and $x = 59$ m. The wave height decay drives a water level set-up (preceded by a set-down in the shoaling region), leading to a positive cross-shore gradient in the mean water level throughout the breaking and inner surf zone (Figure 5a).

3.2. Outer Flow Velocities

Figure 5 shows vertical profiles of time-averaged velocities (plot a) and *rms* periodic velocities (plot b). Although ACVP (near-bed) measurements are included in Figures 5a and 5b, they are discussed separately and in more detail in section 4.

Time-averaged horizontal velocities (Figure 5a) are positive above wave trough level (η_{tr}), highlighting an onshore mass flux, and are negative (offshore-directed) below η_{tr} due to the compensating return current (undertow). The undertow velocity magnitude increases gradually in the shoaling zone (from $x = 51.0$–53.0 m) and more rapidly in the breaking region, particularly along the lee side of the bar (Figure 5a). Maximum undertow velocity magnitudes (up to -0.6 m/s) occur in the breaker bar trough ($x = 56.5$–58.0 m), similar to previous studies involving barred profiles in field [e.g., *Garcez-Faria et al.*, 2000] and laboratory [e.g., *Boers*, 2005] conditions. In the inner surf zone ($x > 58.5$ m), undertow velocity magnitudes reduce. Over the bar crest ($x = 55.0$ m), highest offshore velocities occur in the middle of the water column while at locations around the bar lee side and bar trough the highest offshore velocities occur close to the bed ($x = 56.5$–59.0 m). A more in-depth analysis of the undertow profiles is not considered in the present study, which focuses primarily on the near-bed velocities.

Root-mean-square horizontal periodic velocities ($\tilde{u}_{rms}$) are nearly uniform with depth (Figure 5b), as can be expected in shallow water. Measurements above trough level are not considered, because $\tilde{u}_{rms}$ is undefined when data are discontinuous. $\tilde{u}_{rms}$ is roughly constant between $x = 51$ and 55 m, decreases rapidly between

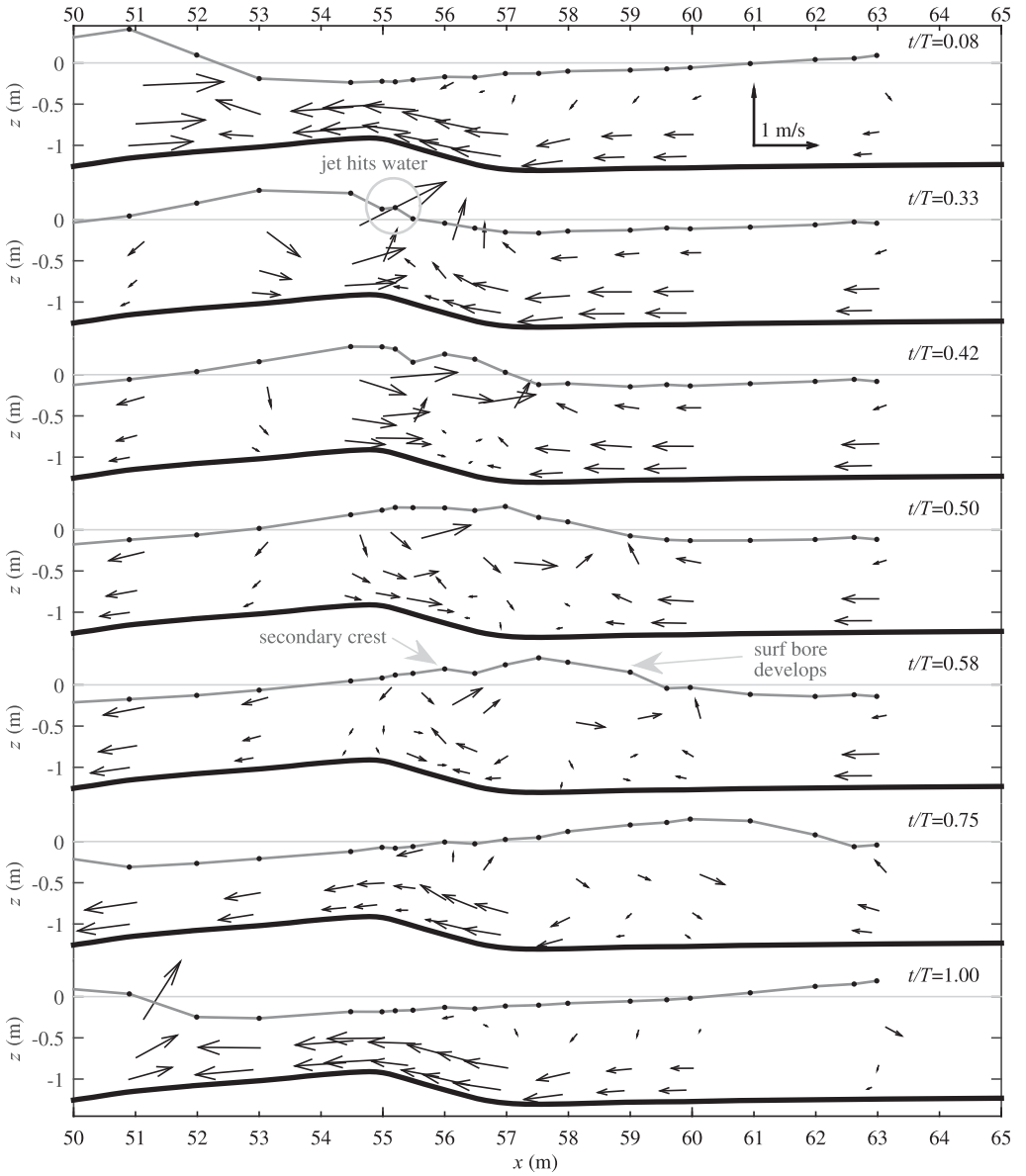

Figure 4. Phase-averaged water surface levels (PT and RWG, grey line plus dots) and velocities (ADVs) at selected phases. Horizontal grey lines mark the SWL ($\eta = 0$) and the thick solid line at bottom marks the reference bed profile.

$x = 55$ and 57 m, and varies hardly throughout the inner surf zone ($x > 58.5$ m). The strong reduction in $\tilde{u}_{rms}$ ($x = 55$–57 m) is consistent with the decay of wave energy and the increased water depth in this region. The distinct near-bed increase in $\tilde{u}_{rms}$ toward the bed at all locations (most evident from $x = 51$ to 55 m) relates to the velocity overshoot in the WBL which will be discussed further in section 4.2.

Figure 4 shows ADV-measured phase-averaged velocities at selected wave phases. As the wave arrives at the test section and travels along the offshore slope and bar crest ($x = 51$–55 m), velocities are in phase with the water surface elevation, i.e., directed onshore under the wave crest and offshore under the wave trough. At wave plunging ($t/T = 0.33$), strong upward-directed velocities under the wave front are evident and agree with earlier observations [e.g., *Ting and Kirby*, 1995]. At the lee side of the breaker bar, the wave orbital motion interacts with the strong undertow. At this location, velocities are directed offshore through almost the complete wave cycle. As the wave crest passes ($t/T = 0.42$–0.58), near-bed velocities become nearly zero due to the counteracting offshore-directed return current and the onshore-directed orbital crest velocities. During the wave trough phase ($t/T = 0.75$–0.2), the combination of the strong undertow and negative orbital velocities results in strong offshore and upward velocities along the bar's lee side.

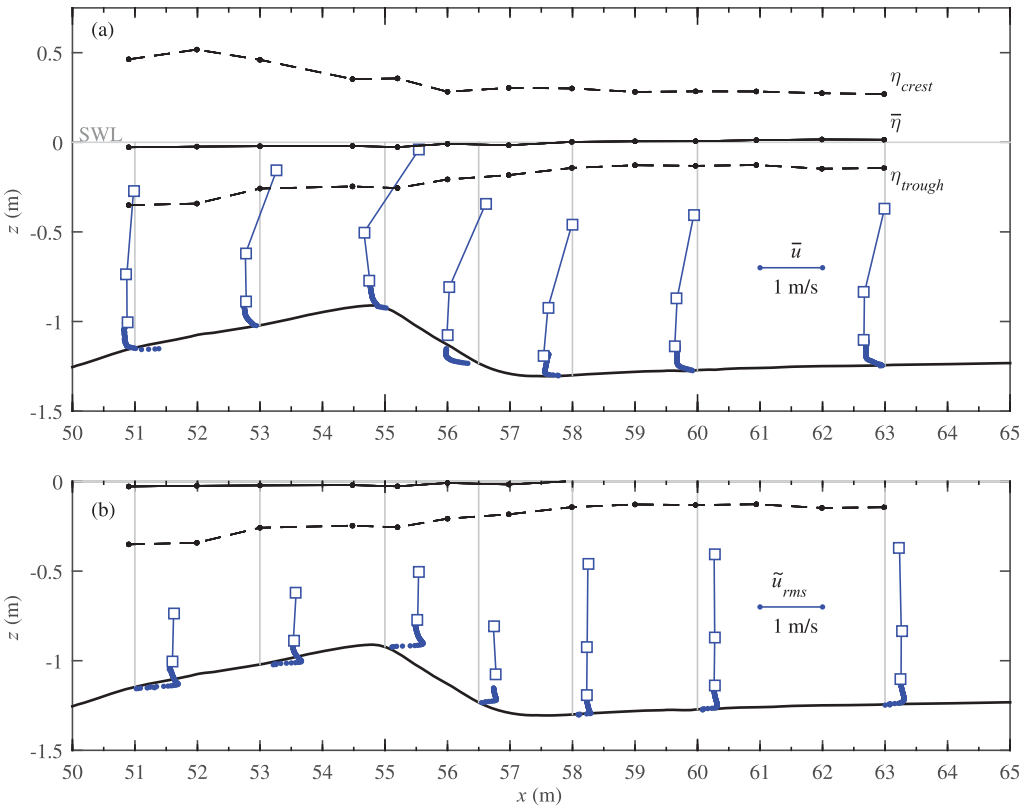

Figure 5. Profiles of (a) undertow and (b) rms periodic velocities, both for t = 0–15 min, measured with ADV (squares) and ACVP (dotted profiles). Both plots include the cross-shore varying wave trough and crest level (black dots and dashed line) and the time-averaged water surface level (set-up/set-down; black dots and solid line).

4. Near-Bed and Wave Bottom Boundary Layer (WBL) Flow

4.1. Phase-Averaged Velocities

Figure 6 shows profiles of ACVP-measured phase-averaged horizontal velocities. Note that the bed was mobile and intrawave bed level variations occurred of *O*(mm). For consistency, $\zeta = 0$ m is set as a constant position for the entire wave cycle equal to the highest intrawave bed level. This level generally occurs around near-bed flow reversal (zero velocity). Due to intrawave erosion of the immobile-bed level, nonzero velocities can be found at $\zeta < 0$ m. As a proxy for the maximum crest-phase WBL thickness we introduce δ, defined as the elevation of maximum *periodic* velocity $\tilde{u}$ at the instance of maximum free-stream velocity (following e.g., *Jensen et al.* [1989]). Note that δ does not need to coincide with the elevation of maximum phase-averaged velocities $<u>$ in Figure 6, as these include the time-averaged velocity contribution $\bar{u}$.

At the four locations at the offshore slope of the bar (x =51.0–55.0 m), the profiles show similar behavior (Figure 6). Since waves are strongly asymmetric (i.e., acceleration-skewed), the trough-to-crest half-cycle is of shorter duration than the crest-to-trough half-cycle. The highest near-bed velocities, exceeding 1 m/s, occur at the most offshore location ($x = 51.0$ m). The overshooting of velocities close to the bed ($\zeta \approx$ 0.02 m) is addressed in the next section.

Periodic velocities are lower along the shoreward-facing slope of the bar and bar trough ($x = 55.5$–58.0 m), consistent with the outer flow observations. At the same time, the offshore-directed return current (undertow) increases. The combined effect yields a reduction in crest velocity magnitudes and in positive (onshore) velocity duration, especially from $x = 56.5$ to 58.0 m, where velocities are negative (offshore) for almost the entire wave cycle. At some locations (e.g., $x = 56.0$ m), velocities are increasingly directed offshore with distance from the bed as the magnitude of $\bar{u}(\zeta)$ increases. These profiles are similar to those previously observed for waves propagating against a steady current [e.g., *Van Doorn*, 1981; *Kemp and Simons*, 1983]. At $x = 57.0$ m, a positive $d<u>/d\zeta$ is observed at elevations slightly above the WBL. This feature

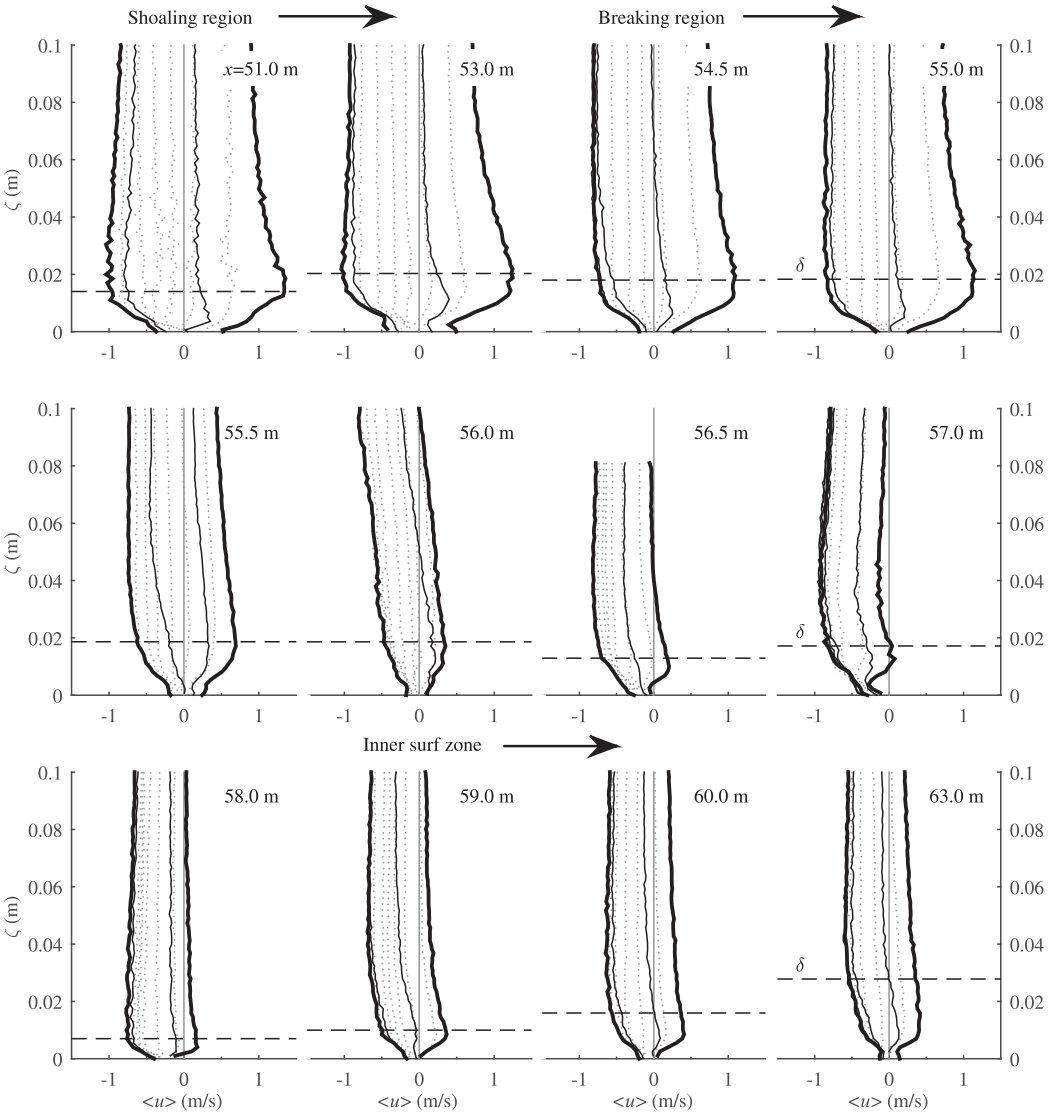

Figure 6. Vertical profiles of phase-averaged horizontal velocity near the bed (ACVP; t = 0–15 min) for 10 phases evenly separated over the wave period. Distinction is made between trough-to-crest half-cycle (thin solid lines) and crest-to-trough half-cycle (dotted lines). Thick solid lines correspond to times of maximum onshore and offshore free-stream velocity. Also included is the maximum boundary layer thickness δ (horizontal dashed line).

differs from previous wave-current studies and relates to the large undertow velocities close to the bed (section 3; Figure 5a). At all locations, crest velocities at the elevation of periodic-velocity overshooting ($\zeta = \delta$) are larger than in the free-stream ($\zeta = 0.10$ m). This can lead to a short duration of onshore velocities at $\zeta = \delta$, even when the free-stream velocity is offshore directed for the entire wave cycle (e.g., at $x = 56.0$ and 56.5 m).

In the inner surf zone, where the orbital velocity amplitude increases and the undertow magnitude decreases (Figure 5 and Table 1), the duration of onshore velocities gradually increases with x-location (Figure 6). Compared to the shoaling and breaking regions, velocity profiles in the inner surf zone are more depth-uniform for $\zeta > \delta$.

4.2. Time-Averaged Velocities

Based on previous work, four main processes may affect time-averaged velocities in the WBL in this experiment: (i) offshore-directed undertow; (ii) onshore-directed progressive wave streaming [e.g., *Kranenburg et al.*, 2012]; (iii) wave shape streaming, offshore-directed for positively skewed/asymmetric waves

[*Trowbridge and Madsen*, 1984; *Fuhrman et al*., 2009b]; and (iv) flow convergence, leading to onshore-directed near-bed streaming at the seaward-facing side of the breaker bar [e.g., *Jacobsen et al*., 2014].

Figure 7 presents the vertical profiles of time-averaged horizontal velocities $\bar{u}(\zeta)$ within and just above the WBL. $\bar{u}(\zeta)$ is presented both with linear (Figure 7a) and logarithmic (Figure 7b) vertical axis, which allows a better comparison with previous WBL studies. All profiles in Figure 7 are scaled with the free-stream velocity at $\zeta = 0.10$ m.

For the most offshore location ($x = 51.0$ m), the profiles in Figures 7a and 7b show four distinct segments: (i) a logarithmic increase (in offshore-direction) in $\bar{u}$ from $\zeta/\delta = 0$–0.5; (ii) a local maximum (in offshore-direction) between $\zeta/\delta = 0.5$–0.8; (iii) a local minimum (in absolute sense) of $\bar{u}$ between $\zeta/\delta = 0.8$ and 1.8; and (iv) nearly depth-uniform $\bar{u}$ from $\zeta/\delta = 2$–5. The profile shape is similar to previous observations under non-breaking waves over a horizontal bed [*Schretlen*, 2012]. *Kranenburg et al*. [2012] showed that this profile shape can be explained through contributions of offshore-directed wave-shape streaming (segment ii) and onshore-directed progressive wave streaming (segment iii).

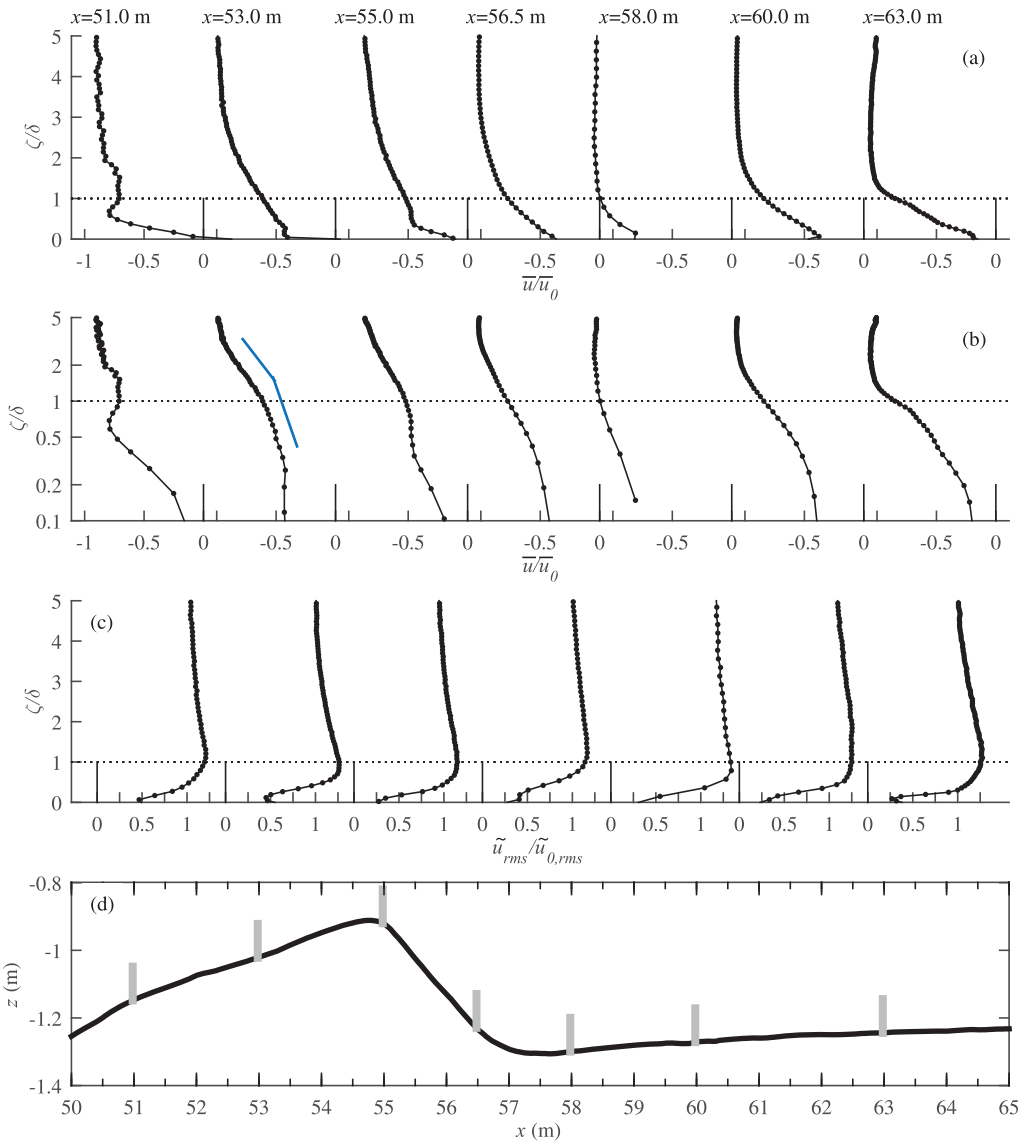

Figure 7. Near-bed horizontal velocity profiles at selected locations. (a) Time-averaged velocities; (b) similar to Figure 7a, but with vertical axis on logarithmic scale. The blue straight lines depict the velocity gradient, with inflection point that is typical for wave-current interactions; (c) Root mean square periodic velocities; (d) Reference bed profile at t = 0 min and measurement locations. All velocities in Figures 7a–7c are scaled with free-stream velocities at $\zeta = 0.10$ m.

At all other cross-shore locations (x>51 m), $\bar{u}(\zeta)$ increases in magnitude with distance from the bed, with no evidence of wave-shape or progressive-wave streaming effects because of the strong undertow. At some locations a double-logarithmic velocity profile is observed, with inflection point above the WBL, as indicated by the blue lines at x=53.0 m (Figure 7b). Such $\bar{u}(\zeta)$ profiles are typically observed in wave-current conditions, obtained from numerical [*Fredsøe*, 1984; *Davies et al*., 1988] and experimental [*Van Doorn*, 1981; *Kemp and Simons*, 1983] studies. At locations with particularly strong undertow relative to the orbital velocity, e.g., at x = 56.5 and 58.0 m (cf., Table 1), the $\bar{u}(\zeta)$ profiles follow a single logarithmic distribution for elevations $0.5\delta < \zeta < 2\delta$ (Figure 7b). This suggests that at these locations, near-bed velocities are dominated by the undertow with minor effect of wave-induced mixing. The double-log profile seems to reestablish at the inner surf zone, suggesting that the orbital motion regains importance in affecting the net currents.

Close to the bed ($\zeta < 0.5\delta$), time-averaged horizontal velocity profiles deviate from a logarithmic profile. This occurs because $\zeta = 0$ is defined as the level of the bed at rest, hence intrawave and time-averaged velocities may still persist at $\zeta < 0$. In addition, for sheet flow conditions (x = 51.0–55.0 m), velocities inside the sheet flow layer do not satisfy the logarithmic distribution [*Sumer et al*., 1996].

4.3. Periodic Velocities and Wave Bottom Boundary Layer Thickness

Figure 8 shows the vertical profiles of horizontal periodic velocity $<\tilde{u}(\zeta)>$ along the offshore slope of the breaker bar. This figure differs from Figure 6 as time-averaged velocities $\bar{u}$ are subtracted. Overshooting occurs at each location during peak offshore and onshore phases and is most prominent during the crest phase. The overshoot is explained by the velocity defect in the WBL behaving as a damped wave that travels upward [*Nielsen*, 1992] and has been observed in boundary layers in oscillating flows [e.g., *Jensen et al*., 1989; *van der A et al*., 2011], under laboratory waves [e.g., *Schretlen*, 2012] and under laboratory spilling waves [*Huang et al*., 2010]. Above $\zeta = \delta$, peak onshore and offshore periodic velocity magnitudes gradually decrease until a near-zero vertical gradient is reached at $\zeta \approx 0.10$ m. For all locations, the periodic crest velocities at $\zeta = \delta$ are considerably (about 50%) higher than at 0.10 m. This is partly attributed to a change in the shape of the periodic-velocity time series as the bed is approached: changing phases of the higher harmonics leads to increasing velocity skewness and decreasing acceleration skewness [*Berni et al*., 2013]. In the present experiment, this shape transformation starts at $\zeta \approx 2$–5δ. Furthermore, the *rms* periodic velocities at $\zeta = \delta$ are notably higher than at 0.10 m (Figures 7c and 5b), leading to a larger orbital excursion and peak onshore and offshore orbital velocities. Such increased $\tilde{u}_{rms}$ at $\zeta = \delta$ relates to the velocity overshooting and is also observed at breaking and inner surf zone locations further shoreward (x > 55.0 m). In the present study, $\tilde{u}_{rms}(\delta)/\tilde{u}_{rms}(5\delta) \approx 1.2$ (+/− 0.1), which is somewhat higher than the value of about 1.07 found with numerical boundary layer models that were validated against laboratory observations for nonbreaking waves [e.g., *Nielsen*, 1992; *Kranenburg et al*., 2012].

The elevation of maximum periodic velocity overshoot during the crest phase is used here as a proxy of the WBL thickness [following *Jensen et al*., 1989]. Previous measurements under velocity-skewed waves above a

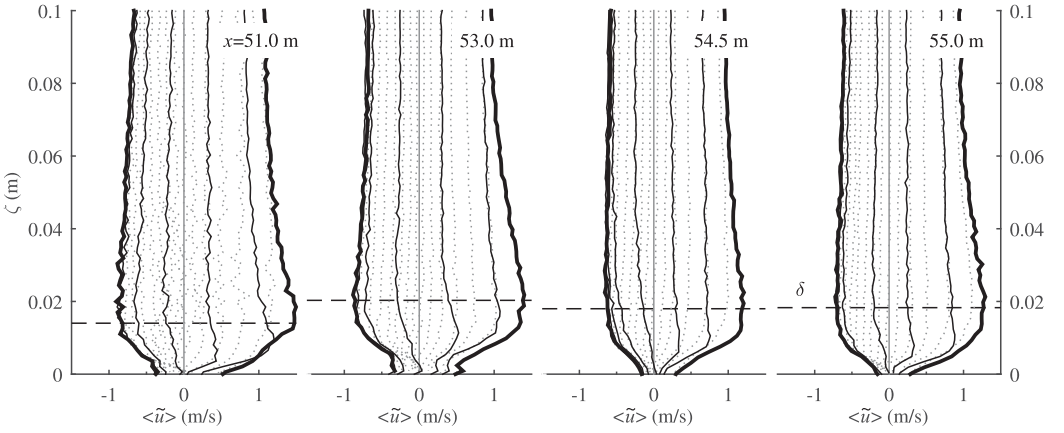

Figure 8. Vertical profiles of phase-averaged horizontal periodic velocity at shoaling locations for 20 phases evenly spread over the wave cycle. Distinction is made between trough-to-crest half-cycle (thin solid lines), the crest-to-trough half-cycle (dotted lines), and instances of peak crest and trough free-stream velocity (thick lines).

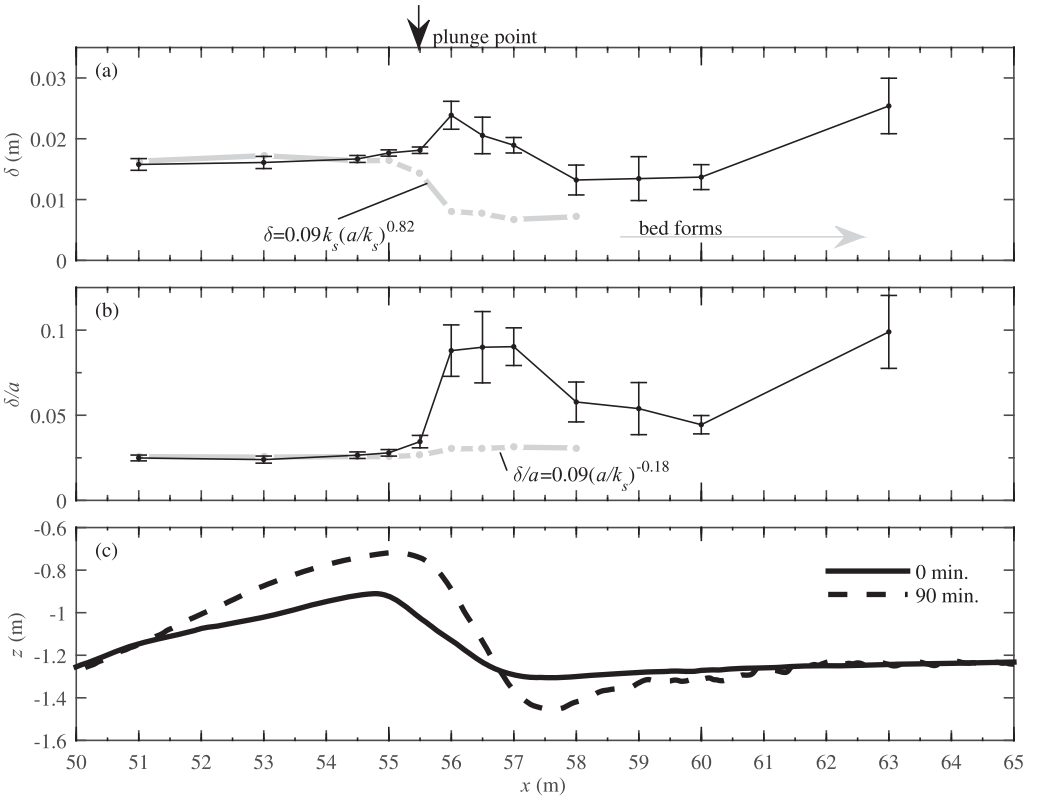

Figure 9. Overshoot elevation (δ), as proxy for WBL thickness, along test section. (a) Dimensional δ; (b) δ/a at $\zeta = \delta$; (c) Bed profiles at start (solid) and end (dashed) of experiment. Values depicted in Figures 9b and 9c are averaged over six runs per location (crosses and black line), with error bars marking +/− one standard deviation of mean. The grey dots and dashed line in Figures 9a and 9b mark the empirical prediction of Fredsøe and Deigaard (1992), equation (6).

mobile bed showed that the overshoot elevation is at higher elevation during the crest phase than during the trough phase, i.e., when highest velocity magnitudes are reached [*Schretlen*, 2012]. In contrast, for positive acceleration-skewed flows, the WBL thickness is smaller during the crest phase since the WBL has less time to develop compared to the trough phase [*van der A et al.*, 2011]. Comparison of the peak onshore and offshore periodic-velocity profiles (Figure 8) shows that the maximum overshoot elevation occurs at a similar level for the crest and the trough phases. A possible explanation is that the opposing effects of velocity and acceleration-skewness on WBL thickness tend to cancel each other out. Approximately similar crest and trough WBL thicknesses were also found at other locations in the breaking and inner surf zones (not included in Figure 8).

Measurements of δ are compared quantitatively with the empirical formulation of *Fredsøe and Deigaard* [1992]:

$$\delta/k_s = 0.09(a/k_s)^{0.82} \tag{6}$$

in which k_s denotes the roughness. Although equation (6) was based on rigid rough-bed experiments, it has been shown to predict reasonably well WBL thickness for mobile-bed sheet flow conditions for a range of sediment sizes in full-scale oscillatory flows [*O'Donoghue and Wright*, 2004; *Campbell et al.*, 2007] and non-breaking progressive surface waves [*Schretlen*, 2012]. In these studies, the roughness was taken as $2.5D_{50}$ rather than relating k_s to the sheet flow thickness. Hence, the roughness k_s is here also set equal to $2.5D_{50}$.

Equation (6) is applied here in a situation with a superimposed current. This can be justified based on the results of *Nielsen* [1992] who analyzed the data set of *van Doorn* [1981] and found no effect of a moderate-strength superimposed current on *rms* periodic velocities (this is further discussed in section 6). Equation (6) is applied only for flat-bed locations, as rippled-bed conditions are considered outside the equation's application range.

The cross-shore variation of δ and predictions of δ using equation (6) are shown in Figure 9a. Note that the measured δ values are averaged over six runs per location and that due to variability of δ between runs, values in Figure 9a may differ slightly from values depicted in Figures 6 and 8.

Between $x = 51.0$ and 55.0 m, δ is almost constant. This may be expected as the free-stream velocities show little cross-shore variation (Figure 5c). The measured δ is in good agreement with predicted δ from equation (6) and, consequently, is in good agreement with δ from previous oscillatory flow mobile-bed experiments. This suggests that flow nonuniformity under progressing surface waves over the sloping bed has little impact on the WBL thickness across the shoaling and breaking locations offshore from the bar crest.

Near the plunge point, along the shoreward slope of the breaker bar, δ increases slightly, even though the periodic-velocity amplitude decreases in this region. Consequently, δ/a increases substantially shoreward from the plunge point (Figure 9b). In addition, measured δ are substantially larger than predicted δ; especially from $x = 56.0$–57.0 m, where the difference exceeds a factor 2. Possible physical explanations for this observation are given in section 6.

Toward the bar trough, both δ and δ/a decrease again. Further into the inner surf zone, at $x = 63.0$ m, δ increases due to an increasing bed roughness in the presence of sand ripples and the associated ripple vortex regime.

5. Turbulence

5.1. Time-Averaged Turbulent Kinetic Energy

Figure 10a shows vertical profiles of time-averaged turbulent kinetic energy (TKE), Froude-scaled ($\sqrt{\bar{k}/gh}$) to enable comparison with previous studies. An offset between the ADV and ACVP-measured TKE becomes apparent and is discussed further in section 6. The down-looking ACVP could induce wake turbulence, leading to enhanced turbulence magnitudes near the sensor. However, no local increase in TKE near the sensor becomes apparent from the figure, and the effect is therefore assumed negligible compared to other sources of TKE.

In the outer flow, TKE decreases from the top of the water column downward. This decay is consistent with many previous breaking-wave studies [e.g., *Scott et al*., 2005; *Yoon and Cox*, 2010], and implies that turbulence production by wave breaking and the surf bore dominates turbulence levels in the upper half of the water column. The cross-shore evolution of TKE in the middle of the water column shows an increase from shoaling zone towards the bar crest, followed by a decay of $\bar{k}$ in the inner surf zone. This pattern is consistent with previous studies involving a barred profile [*Boers*, 2005; *Scott et al*., 2005; *Yoon and Cox*, 2010]. High values at the bar crest relate to wave breaking, while the decrease toward the bar trough and inner surf zone is attributed to an increase in water depth (turbulence spreads over a larger water mass) and reduced wave energy [*Yoon and Cox*, 2010].

At the bar crest, and in the middle of the water column, we find $\sqrt{\bar{k}/gh} \approx 0.043$. This matches well with the magnitude of about 0.04 reported for similar-scale flume experiments involving plunging (but irregular) waves [*Scott et al*., 2005; *Yoon and Cox*, 2010; *Brinkkemper et al*., 2015]. However, $\sqrt{\bar{k}/gh}$ is substantially smaller compared to the plunging wave tests of *Ting and Kirby* [1994] and *Govender et al*. [2002], who found values of about 0.08. In addition, both these studies found $\bar{k}$ profiles that were almost depth-uniform, indicating less decay of TKE with depth compared to the present study and other large-scale experiments. These differences may relate to the smaller scale and the plane sloping bed geometry (i.e., no bar) of *Ting and Kirby* [1994] and *Govender et al*. [2002], leading to relative wave heights H/h near the plunge point that are substantially larger than in the present study.

Figure 10b shows ACVP-measured vertical profiles of $\bar{k}(\zeta)$ inside the WBL, and Figure 10c shows the cross-shore evolution of maximum TKE inside the WBL. Near-bed $\bar{k}$ at the most offshore location ($x = 51.0$ m) is depth-uniform and its magnitude in the WBL is much lower compared to all other cross-shore locations. Apparently, the amount of turbulence produced at the bed is small. Further shoreward ($x = 53.0$ m), $\bar{k}$ magnitudes increase rapidly from the bed upward, reach a maximum at around $\zeta = 0.5\delta$, and decrease at higher elevations. The shape of this profile, with highest values close to the bed, is similar to previous measurements from rigid-bed oscillatory boundary layer experiments where the main turbulence production was due to bed shear [e.g., *Jensen et al*., 1989; *van der A et al*., 2011]. The decrease in $\bar{k}$ for $\zeta < 0.5\delta$ (Figure 10b, $x = 53.0$ m) is not consistent with results from rigid-bed experiments, for which the highest values of $\bar{k}$ are typically found much closer to the bed. This difference may be due to physical processes in mobile bed

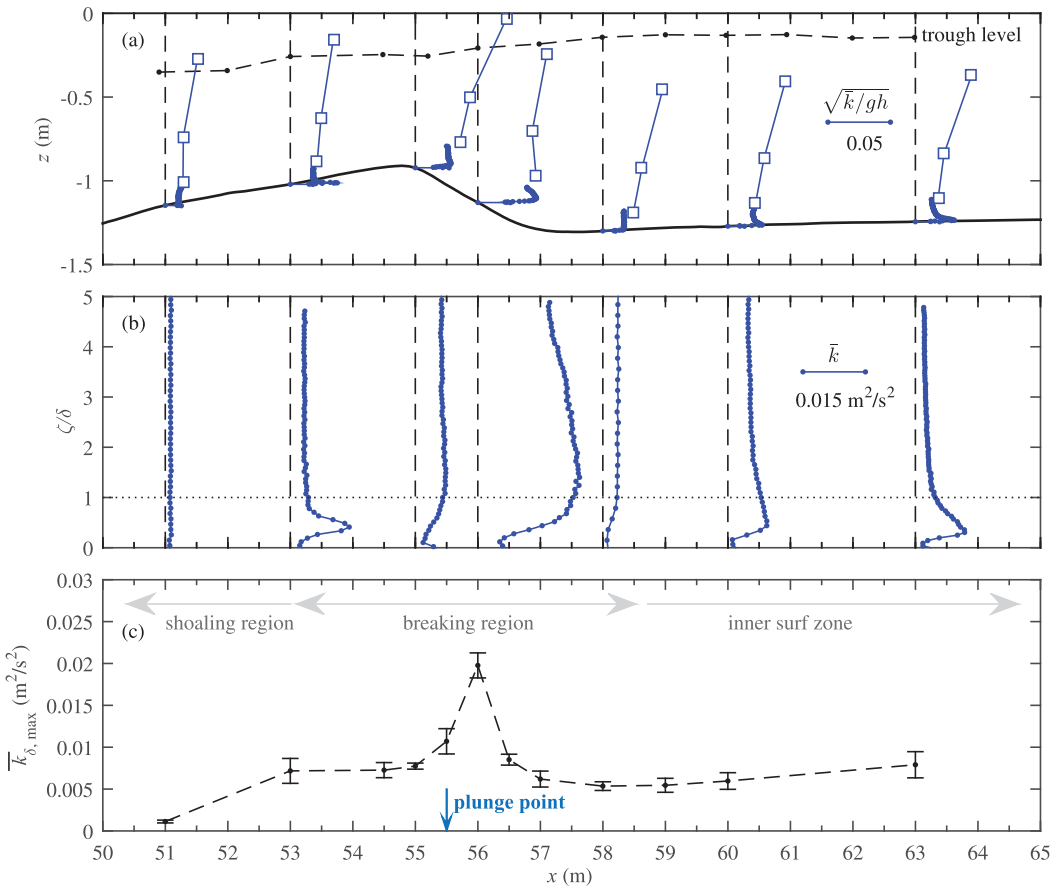

Figure 10. Time-averaged TKE, measured with ADVs (squares) and ACVP (dots). (a) Froude-scaled TKE over complete water column; (b) close-up of TKE profiles near the bed and in the WBL; (c) Maximum time-averaged TKE measured in the WBL, mean (dots and dashed line) +/− standard deviation of mean (error bars).

conditions, such as turbulence damping [*Dohmen-Janssen et al*., 2001; *Hsu et al*., 2004] or reduced turbulent mixing efficiency in the dilute suspension layer above a dense bedload layer [*Revil-Baudard et al*., 2015]. However, instrument limitations (Appendix A) may also be a factor. The strong increase in $\overline{k}_{\delta,\max}$ at $x = 53.0$ m relative to $x = 51.0$ m, for the complete near-bed layer including the WBL (Figure 10c), is remarkable since magnitudes of free-stream velocities are similar at both locations (Table 1). This suggests that turbulence at $x = 53.0$ m is not only produced locally at the bed and that there is a significant contribution of breaking-generated turbulence that arrives at this location.

In the breaking region at $x = 55.0$ and 56.0 m, the near-bed $\overline{k}$ profiles are more depth-uniform without a distinct maximum within the boundary layer. The vertical distribution and the magnitudes of $\overline{k}$ suggest that TKE generation by bed friction is small compared to contributions of breaking-induced turbulence. Magnitudes of TKE increase from shoaling to breaking zone for the complete near-bed region including the WBL (Figure 10c). Of particular note is the increase in $\overline{k}_{\delta,\max}$ near the plunge point around the breaker bar crest (a factor 2.7 increase from $x = 54.5$ to 56.0 m), despite the strongly decreasing peak onshore and offshore near-bed velocities in this region (Table 1). The bed is plane in this region, which excludes an increase in TKE due to small-scale bed forms. The strong undertow current at these locations is expected to have a minor effect on local turbulence values. This was shown previously in experiments with waves and superimposed current for which $\overline{k}$ values were not much larger compared to the same waves without a current [cf., *Kemp and Simons*, 1983]. Hence, results indicate that the substantial increase in $\overline{k}_{\delta,\max}$ in the breaking zone is primarily caused by breaking-induced turbulence that invades the WBL.

In the bar trough ($x = 57.0$–59.0 m), magnitudes of $\overline{k}_{\delta,\max}$ are significantly lower than at bar crest locations but are nevertheless notably higher than in the shoaling zone (cf., $x = 51.0$ m). The latter suggests that

breaking-generated turbulence still reaches the bed in the bar trough, despite the much larger vertical distance between water surface and bed compared to bar crest locations. The vertical profile of near-bed $\bar{k}(\zeta)$ at $x = 58.0$ m is almost depth-uniform (Figure 10b). The absence of a near-bed increase in $\bar{k}(\zeta)$ suggests that bed shear by orbital velocities does not add significantly to local TKE. However, bed shear by time-averaged velocities (undertow) may result in similar depth-uniform profiles [see e.g., *Sleath*, 1991] and may therefore contribute to near-bed TKE in the bar trough. Vertical profiles of $\bar{k}(\zeta)$ in the inner surf zone ($x > 58.5$ m) show that bed-generated turbulence due to orbital-velocity shear gradually regains importance. Throughout the inner surf zone, $\bar{k}_{\delta,\max}$ increases due to increasing bed form roughness (Figure 10c).

5.2. Time-Varying Turbulent Kinetic Energy

Figure 11 shows detailed measurements of $<k>$ inside the WBL and in the layer immediately above it ($\zeta/\delta = 0$–5). A dominance of bed-generated turbulence in near-bed time-varying $<k>$ occurs at locations relatively far from the plunge point, i.e., at $x \leq 54.5$ m and at $x > 58.5$ m. At $x = 53.0$ and 54.5 m, large turbulent events are formed at the bed during instances of peak trough and crest velocities. The bed-generated TKE remains confined to the WBL at $x = 53.0$ m, but appears to diffuse outside the WBL at $x = 54.5$ m. Bed-generated TKE at the inner surf zone ($x > 58.5$ m) is particularly observed during the crest phase. Turbulence production at the bed occurs due to the presence of vortex ripples in the inner surf zone which increase

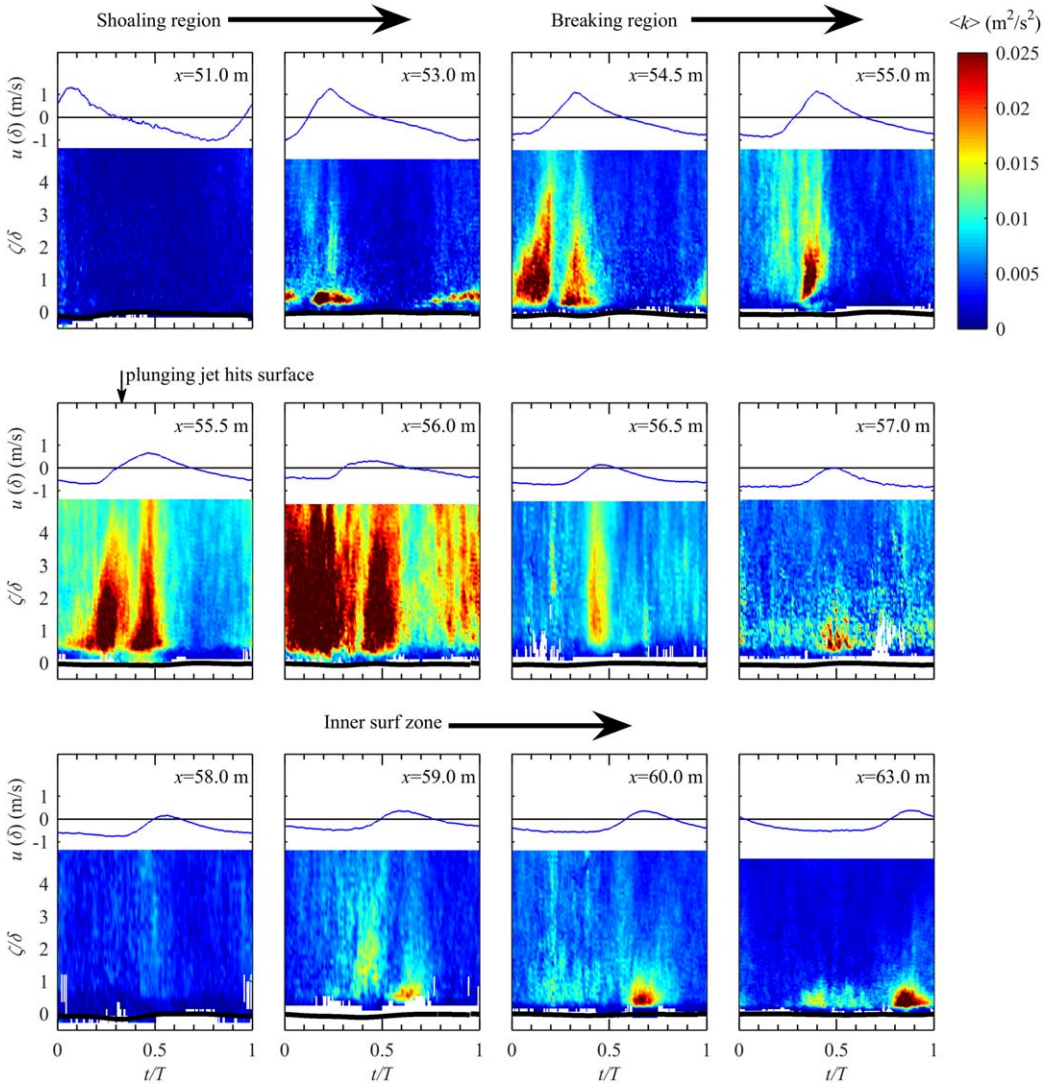

Figure 11. Time-varying turbulent kinetic energy <k> near the bed, measured by ACVP for t = 0–15 min. Free-stream horizontal velocities at $\zeta = \delta$ are included in each plot as a reference.

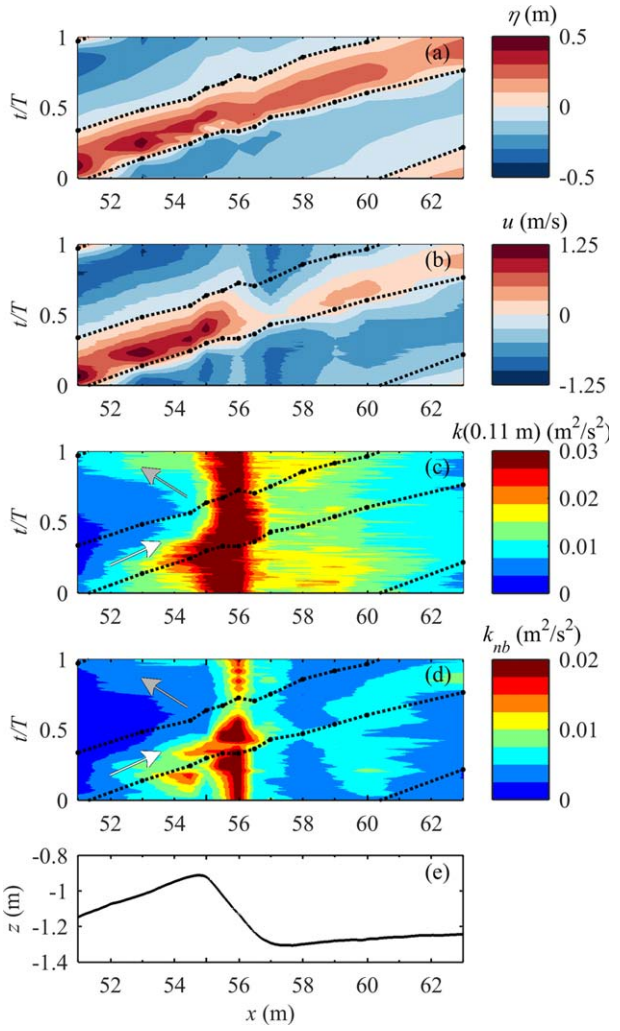

Figure 12. Surface plots of spatial (horizontal axis) and temporal (vertical axis) variation of (a) Water surface levels; (b) Horizontal velocities at $\zeta = \delta$; (c) TKE, measured by ADV at $\zeta = 0.11$ m; (d) Near-bed TKE, measured by ACVP, depth-integrated over the lowest 0.10 m (k_{nb}). Dashed lines depict zero crossings of η. Arrows in Figures 12c and 12d are explained in main text. Figure 12e shows the reference bed profile.

the bed roughness. At these inner surf zone locations, similar to $x = 53.0$ m, bed-generated TKE remains largely confined to the WBL.

Breaking-generated turbulence affects time-varying near-bed $<k>$ at locations close to the plunge point at $x = 55.5$ m. At $x = 55.5$–56.0 m, i.e., roughly below the plunge point and close to the bar crest, $<k>$ increases during the early crest phase ($t/T = 0.4$–0.6). This increase occurs rapidly and uniformly over the complete near-bed layer, which indicates that the source is breaking-induced TKE that comes from above and mixes rapidly over the near-bed layer. This peak in TKE lags the instance of the plunging jet hitting the water (at $x = 55.5$ m and $t/T \approx 0.33$) by $\Delta t \approx 0.5$ s ($\Delta t/T \approx 0.1$–0.2). At $x = 56.0$ m, $<k>$ increases a second time during the wave trough phase ($t/T = 0$–0.3), marking a second event of turbulence arrival. A trough-phase increase in TKE can also be identified at $x = 55.5$ m, particularly when focusing on elevations outside the WBL ($\zeta = 4$–5δ). Closer to the bed at $x = 55.5$ m, bed-generated turbulence merges with breaking-induced TKE, leading to maximum $<k>$ values that are much higher than at offshore locations with similar near-bed velocities ($x = 53.0$–55.0 m).

Offshore from the plunge point, at $x = 55.0$ m, a sudden increase in TKE above the WBL during the end of the wave trough phase ($t/T = 0.2$) can be identified. This increase is rather uniform over depth, suggesting that this TKE is not produced locally at the bed but relates instead to the arrival of breaking-induced turbulence. After passage of the wave crest ($t/T = 0.4$), TKE decreases depth-uniformly. Shoreward from the region of high turbulence below the plunge point, at $x = 56.5$ m, $<k>$ increases rapidly during the crest phase ($t/T = 0.4$–0.5). Again, the depth-uniformity of this increase suggests that it is not due to local turbulence production at the bed. Further shoreward, in the region covering the lower lee-side of the breaker bar and the bar trough ($x = 57.0$–58.0 m), the limited temporal variation of TKE indicates that there is little turbulence production by wave-related bed shear and limited arrival of advected breaking-induced TKE.

Due to strong cross-shore gradients in near-bed TKE, the temporal behavior seen in Figure 11 is not fully explained by local processes, i.e,. production at the bed or at the water surface and advection/diffusion in vertical direction only. Instead, we may expect significant contributions of horizontal turbulence advection to the temporal variation of near-bed TKE. The horizontal TKE advection is seen in Figure 12c, which shows the spatiotemporal variation of TKE at $\zeta = 0.11$ m. The continuously high near-bed TKE magnitudes at $x = 55.5$ and 56.0 m stand out. Along the offshore slope of the bar ($x = 51.0$–55.0 m), the highest TKE values are found during the zero-up crossing of the surface elevation. This relates not only to production at the bed (Figure 11), but also to the arrival of TKE generated below the plunge point which is advected offshore

by orbital and undertow velocities during the trough phase. The latter is identified as a patch of high TKE that travels offshore from the plunge point at $x = 55.5$ m to the shoaling zone at $x \approx 52.0$ m (Figure 12c, grey arrow). After flow reversal to positive velocities, the arriving fluid at shoaling locations comes from $x < 52.0$ m and is relatively low in TKE. Consequently, net advection of TKE is onshore (white arrow in Figure 12c) leading to a decrease in TKE at shoaling locations.

An excursion of TKE also occurs from the plunge point to onshore locations, although the horizontal extent over which TKE is advected is much more restricted, and consequently, the effect is much less apparent. In Figure 12c, the onshore excursion is observed as the patch of high TKE at $x = 55.0$–56.0 moves slightly onshore to $x = 56.5$ m around $t/T = 0.4$, and back offshore around $t/T = 0.6$. The effect is also observed in Figure 11 as a depth-uniform increase in $<k>$ during this time interval. The reduced orbital amplitude and the strong offshore-directed undertow velocity lead to a short duration of onshore-directed phase-averaged velocities in this region, and consequently, restrict the onshore and downward transport of TKE along the shoreward slope of the bar.

Figure 12d shows the spatiotemporal variation of depth-averaged (over $\zeta = 0$–5δ) near-bed TKE (annotated k_{nb}), which resembles the behavior at $\zeta = 0.11$ m. Hence, also in the WBL, cross-shore advection of breaking-generated turbulence has a significant effect on $<k>$. Differences between Figures 12c and 12d are mainly attributed to contributions of bed-generated turbulence to k_{nb} (Figure 11).

5.3. Reynolds Shear Stress

Figure 13 shows the Reynolds shear stress ($-\rho<u'w'>$) at $\zeta = \delta$. The Reynolds shear stress at the bed ($\zeta = 0$) could not be resolved due to instrument limitations (Appendix A).

In the vicinity of the plunge point (at $x = 55.5$ m $+/-$ 0.5 m), peak onshore and offshore Reynolds stresses are found to increase rapidly, with a factor two increase relative to $x = 54.5$ m. The increase is likely associated with the effects of breaking-induced turbulence that reaches the bed, because peak onshore and peak offshore velocities decrease between shoaling and breaking zone (Table 1). Indeed, the increase in onshore/offshore Reynolds stresses occurs in approximately the same region where TKE in the WBL was observed to increase (cf., Figure 10a). Further shoreward ($x = 56.5$–57.0 m), Reynolds shear stresses are almost continuously directed offshore, similar to the near-bed velocities at these locations. The time-averaged Reynolds stresses (crosses in Figure 13) are predominantly negative, which is explained by the negative time-averaged near-bed velocities.

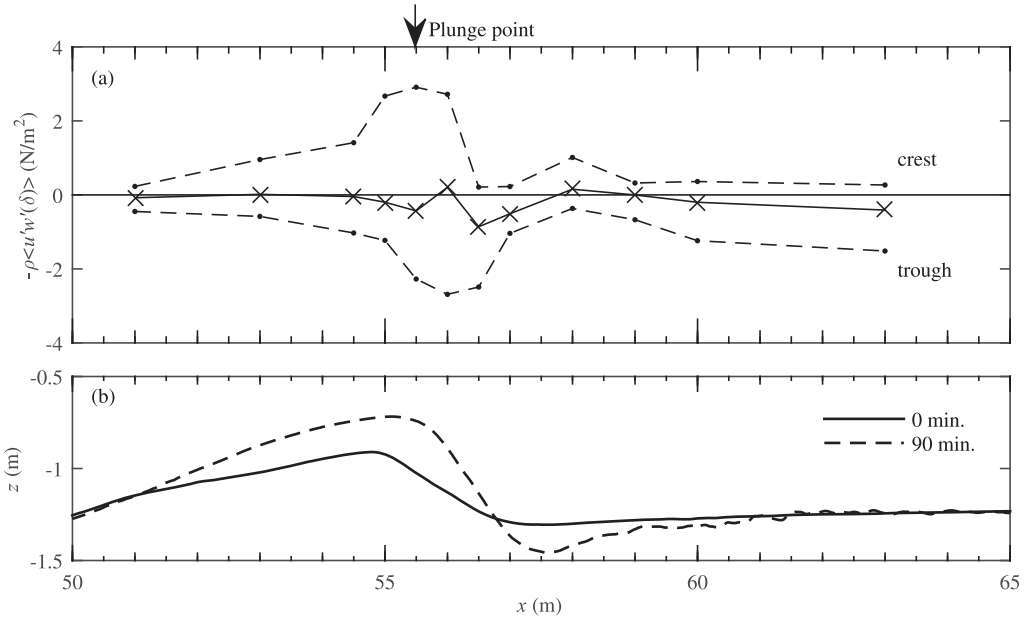

Figure 13. Near-bed Reynolds stresses at $\zeta = \delta$, averaged over t = 0–90 min. (a) Time-averaged (crosses and solid line) and phase-averaged peak onshore and offshore (dots and dashed lines) Reynolds stresses; (b) Bed profiles at t = 0 min. (solid line) and t = 90 min. (dashed line).

6. Discussion

Offsets between ADV- and ACVP-measured $\bar{k}$ can be seen in Figure 10a. Whether these shifts are attributed to differences between ADV and ACVP measurement resolution, differences in acoustic frequencies and associated sensitivity to different particle sizes, slight differences in system orientation relative to the local bed slope (ADV data have not been corrected) or even invalid TKE approximation for the 2C-velocity measurement of the ACVP (see section 2.5), is difficult to determine. Because the ACVP measures systematically lower $\bar{k}$ than the ADV, the discrepancies might be attributed to the lack of spatial-temporal resolution of the ACVP, enhanced by the application of the Doppler noise correction method (Appendix A).

For the same reason, the ACVP-measured Reynolds shear stress (section 5.3) may also underestimate the actual fluid shear. It is not expected that this underestimation varies along the bed profile since the same ACVP settings were used throughout the experiment. Nevertheless, for this reason, a quantitative analysis of the different terms contributing to the total bed shear was not carried out. It should be noted that the Reynolds shear forms only one component of the total bed shear. The time-averaged and periodic velocities can also contribute to—and even dominate—bed shear in the surf zone [*Chassagneux and Hurther*, 2014].

The present results highlight an important contribution of breaking-induced turbulence to TKE inside the wave boundary layer. This agrees with other large-scale laboratory [*Scott et al*., 2005] and field [*Grasso et al*., 2012] studies over a barred profile that included measurements of velocities within, or close to, the WBL. The WBL invasion of breaking-generated turbulence is most apparent at the bar crest and near the plunge point, where TKE increases after arrival of a highly turbulent water body that follows rapidly (about 0.5 s) after the plunging jet strikes the water column (Figure 11, $x = 55.5$–56.0 m). This is consistent with previous studies that showed rapid downward turbulence transport under plunging breakers, associated with large vortices below the wave front [*Ting and Kirby*, 1995; *Christensen and Deigaard*, 2001; *Kimmoun and Branger*, 2007]. It is expected that in the present study the rapid mixing of TKE over the complete water column including the WBL is partly facilitated by the shallow water depths at the bar crest. This suggests that the barred bed profile and cross-shore-varying water depth are important factors controlling the extent to which breaking-induced TKE can reach the WBL.

Breaking-induced TKE is not fully determined by local vertical processes, i.e., production, dissipation, and vertical advection and diffusion. Instead, breaking-generated turbulence travels offshore, leading to an increase in phase and time-averaged TKE over the complete water column including the WBL up to about 3 m offshore from the plunge point. The phase-dependency of the excursion suggests that transport of TKE is advective and links closely to the orbital motion. The distance over which TKE is advected (3 m) equals approximately 6 times the semi-excursion length a and it corresponds to about 15 s ($3 \cdot T$) of advection by offshore-directed time-averaged velocities. This suggests that offshore TKE advection occurs over multiple wave cycles and that breaking-generated TKE does not dissipate within one wave cycle. At the same time, previous research has shown that turbulence transport under plunging waves is not fully advective; diffusive transport may also be important [e.g., *Ting and Kirby*, 1995]. A more detailed analysis of turbulence transport mechanisms is not considered here due to the relatively limited spatial coverage of outer flow velocity measurements. Results of an accompanying rigid-bed experiment involving similar wave conditions and barred profile are expected to extend insights into the TKE transport mechanisms.

The increase in near-bed Reynolds shear stresses in the breaking region agrees qualitatively with previous observations of enhanced bed shear in the breaking region [*Cox and Kobayashi*, 2000; *Sumer et al*., 2013] or under external-grid turbulence [*Fredsøe et al*., 2003]. Quantitative comparisons between these previous studies are difficult, because of significant differences in scale, bed geometry, breaking intensity, and instrumentation (i.e., the Reynolds stress in the present study differs physically from the total bed shear). It was shown by *Fredsøe et al*. [2003] that external turbulence may increase the apparent bed roughness and the WBL thickness. This raises the question to what extent the present study's distinct increase in δ/a (factor 2–3 compared to previous studies) in the breaking region (Figure 9, from $x = 56.0$ to 57.0 m) relates to breaking-induced turbulence or other factors. Three factors are discussed here.

Fredsøe et al. [2003] showed that external turbulence may enhance the turbulent exchange of momentum between free-stream flow and the WBL, resulting in larger wave friction factors over a wide range of Reynolds regimes ($O(Re) = 10^4 - 10^6$). This leads to an increase in apparent bed roughness and an upward displacement of periodic velocity in the inner WBL, similar to how wave-induced mixing can affect steady current profiles [*Fredsøe et al*., 2003]. In addition, the invasion of external turbulence leads to an earlier transition to turbulence in the WBL, which can increase δ/a with as much as a factor 2. Reynolds stresses (Figure 13) suggest a similar enhanced momentum exchange between WBL and outer flow in the present study ($x = 55.0$–56.5 m) which is likely to affect velocity distributions inside the WBL. Whether this effect can explain the significant increase in δ/a cannot be concluded by quantitative comparison with results by *Fredsøe et al*. [2003], because their results were obtained for a smooth bed which differs substantially from hydraulically rough conditions in terms of turbulence intensities and Reynolds stresses at elevations close to the bed ($\zeta < \delta$) [cf., *Jensen et al*., 1989].

A second factor that may affect the WBL thickness is time-averaged undertow velocity, that is particularly strong (relative to periodic velocity) from $x = 56.5$ to 58.0 m. *Nielsen* [1992], using the data set of *van Doorn* [1981] that included values of relative current strength to *rms* periodic velocity ($|\bar{u}|/\tilde{u}_{rms}$) up to 1.11, found no effects of the superimposed current on WBL thickness. In the present study, locations from $x = 56.5$ to 58.0 m have $|\bar{u}|/\tilde{u}_{rms}$ values that exceed 1.11 (Table 1). However, based on the results of *Nielsen* [1992], we deem that the superimposed current cannot explain the strong (factor 3) enhancement of WBL thicknesses in the present study. In addition, the enhanced WBL thickness is observed already at $x = 56.0$ m, where the undertow strength is of moderate strength compared to periodic velocities ($|\bar{u}|/\tilde{u}_{\mathrm{rms}} < 1.11$).

A third factor that potentially affects WBL thicknesses is the bed geometry. *Sumer et al*. [1993] showed that the WBL thickness for converging/diverging flow may differ substantially from uniform flow conditions. In a tunnel with 0.20 m flow depth and with a local bed slope of 1°, the maximum WBL thickness during a diverging flow can be almost twice as thick as a WBL above a uniform (zero inclination) bed [*Sumer et al*., 1993]. In the present experiment, the maximum WBL thickness is estimated during the crest phase when the flow indeed diverges. One may expect that the importance of this effect depends on a relative vertical divergence rate during a wave cycle, i.e., the vertical expansion during the orbital motion relative to the local water depth. This can be expressed as a ratio $a \cdot \tan(\beta)/h$, in which a is the semi-excursion amplitude, β is the local slope, and h is the water depth [cf., *Fuhrman et al*., 2009a]. In *Sumer et al*. [1993], this divergence ratio is approximately 0.26 ($a = 3.0$ m). In the present experiment, along the lee side of the bar at $x = 56.5$ m, this ratio equals about 0.06 at the start of the experiment ($a = 0.31$ m, $\beta = 11°$, $h = 1.1$ m; Table 1) and about 0.12 at the final stage of bar development (as β increases to 25°). Based on this, we may expect flow divergence effects in the present study to be smaller but of same order of magnitude as the experiments of *Sumer et al*. [1993]. Hence, effects of flow divergence on WBL thickness along the shoreward bar slope cannot be dismissed.

The high contributions of breaking-induced turbulence to TKE in and just outside the WBL may have important implications for sediment transport. Not only is turbulence able to entrain sediment from the bed into suspension [*Sumer and Oguz*, 1978], it has also the ability to increase bedload transport [*Sumer et al*., 2003]. The effects of breaking-induced turbulence on suspended and bedload sediment transport processes will be addressed in a forthcoming paper.

7. Conclusions

The present study examines velocities and turbulence dynamics near a sand bed under near-full-scale, plunging breaking waves in a laboratory wave flume. In contrast with previous experiments, detailed measurements were obtained inside and directly above the wave bottom boundary layer (WBL) with high spatial and temporal resolution. These measurements were taken along a mobile sandy breaker bar at shoaling, breaking, and inner surf zone locations. The following conclusions are made:

1. Phase-averaged WBL velocities show similar behavior to nonbreaking and oscillatory WBL studies, including distinct velocity overshooting. Time-averaged velocities in the WBL are largely dominated by the strong undertow and show consistent behavior with previous observations for wave-current interactions.

Wave (shape) streaming mechanisms, as usually observed for uniform nonbreaking waves, are evident only in the shoaling region where the undertow is relatively weak.

2. The dimensionless WBL thickness along the offshore slope of the breaker bar agrees with previous mobile-bed oscillatory flow studies, suggesting that wave nonuniformity does not affect the WBL thickness. However, near the breaking-wave plunge point and along the shoreward slope of the bar, δ/a is about 3 times higher than predictions based on uniform oscillatory flows. This can be attributed to the combined effects of breaking-induced turbulent kinetic energy (TKE) and flow divergence induced by the bed geometry.
3. Outer flow TKE observations match with previous breaking-wave studies, showing highest values in the breaking region at the breaker bar crest, followed by a decrease in the bar trough. In close vicinity of the plunge point (+/− 0.5 m), TKE is almost depth-uniform over the complete water column (including the WBL), indicating large turbulence production and a strong penetration into the water column down to the bed. At shoaling and inner surf zone, vertical profiles of TKE show that also bed-friction is a significant source of near-bed turbulence.
4. Near the plunge point, TKE enters the boundary layer during two instances of the wave cycle: a first occurrence rapidly (about 0.5 s) after wave plunging, when breaking-induced TKE rapidly saturates the complete water column including the WBL; a second occurrence during the wave trough phase, when undertow and periodic velocities transport TKE towards the breaker bar. This invasion results in an increase in maximum TKE inside the WBL with a factor of almost three between shoaling and breaking region, despite decreasing near-bed velocity magnitudes.
5. Breaking-generated turbulence travels horizontally offshore (during trough phase) and back onshore (during crest phase) between breaking and shoaling zone, leading to increased phase and time-averaged TKE over the near-bed region (including the WBL). Hence, the area affected by breaking-generated turbulence is not restricted to the breaking region itself, but extends to shoaling locations about 3 m offshore from the plunge point. Advection of TKE from plunge point in onshore direction is restricted by the combination of a decreased orbital velocity amplitude and strong offshore-directed undertow velocities.
6. Wave breaking affects near-bed Reynolds shear stresses, leading to an increase in maximum onshore and offshore phase-averaged Reynolds stresses at the WBL overshoot elevation. The effect is mostly apparent for the region comprising +/− 1 m around the plunge point, where phase-averaged Reynolds stress magnitudes are a factor 2 higher than at shoaling locations at the bar crest.

Appendix A: Additional Information on ACVP Measurements and Data Treatment

Additional data treatment was required for ACVP-measured turbulence. An example spectrum of ACVP-measured horizontal velocities is shown in Figure A1. A contribution of Doppler noise appears as a deviation from the −5/3 slope that is expected at inertial subrange frequencies. In the present measurement conditions, this Doppler noise is caused by a lack of suspended particles as acoustic targets. Noise contributions are higher at shoaling than surf zone locations, as more sediment grains are entrained in the breaking and inner surf zone regions.

A two-step correction was applied to reduce the Doppler noise contribution. First, data were despiked by applying a moving median with a window width of five samples. Figure A1 shows that this step importantly reduces energy at frequencies contaminated with Doppler noise ($f > 5$ Hz). Second, phase-averaged turbulent intensities were calculated using a two-point cross-correlation method as proposed by *Garbini et al.* [1982]:

$$<u'_{\mathrm{rms}}(z,t)> = \sqrt{<u'(z-\Delta z,t)u'(z+\Delta z,t)>} \tag{A1}$$

This method is based on the assumption that the most energetic turbulent eddies are larger than the separation distance $2\Delta z$, with Δz equal to the ACVP's vertical resolution (1.5 mm). Consequently, the uncorrelated velocity fluctuations constituted mainly by Doppler noise do not contribute to the turbulence covariance given by equation (A1). This method was previously applied successfully in *Hurther and Lemmin* [2001, 2008] in shear and purely diffusive turbulent flows to supress the Doppler noise contribution in the normal Reynolds stress and TKE profile measurements. Figure A1 shows that the applied

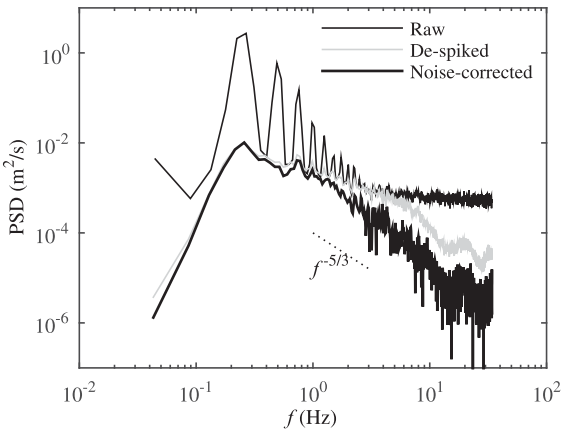

Figure A1. Spectra of horizontal velocity measurements by ACVP at edge of boundary layer ($\zeta = \delta$), shoaling region. Figure includes autospectrum of raw data (thin black line), autospectrum of decomposed turbulent signal after applying despiking through moving median (grey line), and crossspectrum of turbulent velocities at $\zeta = \delta - \Delta z$ and $\zeta = \delta + \Delta z$, equivalent to equation (A1) (thick black line).

cleaning methodology effectively removes Doppler noise, as the cleaned turbulent velocity spectrum follows the expected −5/3 slope in the inertial subranges. Although Doppler noise was largely restricted to the horizontal velocity measurements (due to the strong geometrical weighting) [cf, *Hurther and Lemmin*, 2001], equation (A1) was also applied to the vertical turbulent velocities w'_{rms} for consistency.

In terms of noise effects on Reynolds stresses, previous research found that Doppler noise is intrinsically uncorrelated in the horizontal and vertical directions [*Hurther and Lemmin*, 2001]. However, this is only true if the transmission direction of the ACVP is normal to the local bed slope. As this is not the case in the present experiment, equation (A1) is similarly applied to the Reynolds shear stress using a centered scheme version:

$$-\langle u'w'(z,t)\rangle = -0.5[\langle u'(z-\Delta z,t)\,w'(z+\Delta z,t)\rangle + \langle u'(z+\Delta z,t)\,w'(z-\Delta z,t)\rangle] \quad \text{(A2)}$$

The Reynolds shear may be affected by contributions of wave velocities that are still present in u' and w' after the Reynolds decomposition (see section 2.5). *Feddersen and Williams* [2007] proposed testing of wave bias effects on $u'w'$ using the cumulative distribution of the cross spectrum of u' and w' (ogive curves). Wave bias appears in the ogive curves as a local increase in curve steepness around frequencies associated with the waves. The curves were calculated following the mathematical expression by *Feddersen and Williams* [2007] for each individual run. Following previous studies in field [*Feddersen and Williams*, 2007; *Ruessink*, 2010] and laboratory [*Brinkkemper et al.*, 2015] surf zones, the Reynolds stresses were removed from the analysis if the ogive curves exceeded limits of −0.5 and +1.6 at any frequency or when visual inspection of the curves revealed a dominance of wave contributions to Reynolds shear. In total, 9 out of 72 runs failed the ogive test and were excluded. The exclusion of these runs did not significantly alter the results.

In order to interpret the ACVP data properly, a few considerations regarding the estimates of turbulence quantities from the ACVP measurements are addressed. First, the ACVP measures velocities of sand grains as the dominant source of acoustic scattering. Depending on the local hydrodynamic conditions, the particle velocity may lag the fluid velocity due to particle inertia effects. Consequently, the near-bed turbulence data provided by the ACVP might differ from pure fluid turbulence data. Unfortunately, to our knowledge, this measurement limitation cannot be overcome presently in the absence of instrumentation capable of measuring fluid-velocity data under such dense water-sediment mixtures. Second, application of equation (A1) also eliminates the fraction of TKE contained in eddies smaller than the separation distance $2\Delta z$. However, while the noise correction reduces spectral energy at inertial subrange frequencies ($f > 1$ Hz), the energy associated with the larger energy-containing vortices that contribute most to TKE ($f \approx 0.25$–1.0 Hz) is hardly affected (Figure A1). Third, inside the WBL, the size of eddies reduces significantly within proximity of the bed. These small-scale turbulent eddies may not be properly resolved by the ACVP due to a lack of spatial-temporal resolution [*Soulsby*, 1980]. This may lead to an underestimation of turbulence intensities; especially for the vertical turbulent fluctuations w', which in the vicinity of the bed exhibit much smaller turbulent scales than u' [*Soulsby*, 1980]. At the same time, near-bed TKE is dominated by strongly anisotropic eddies with u'_{rms} much larger than w'_{rms} [*Cox and Kobayashi*, 2000]. As a result, TKE is not severely underestimated by the ACVP. In order to quantify the underestimation, a comparison was carried out between the ACVP and a two-component LDA system (with a roughly 4 times higher spatial-temporal resolution), simultaneously deployed in an equivalent clear-water wave experiment over a rigid bed. The ACVP measurements showed an underestimation in $\sqrt{k}/u_{\max}$ of 10 to 15% at a distance $\zeta = 8$ mm above the rigid bed

(corresponding to about half the WBL thickness). The spatial averaging effect on Reynolds stress measurements is supposedly limited due to the much larger size of shear-producing eddies—typically of the order of the WBL thickness [*Soulsby*, 1980].

Acknowledgments
The authors wish to thank the staff of CIEMLAB, in particular Joaquim Sospedra, Oscar Galego, and Ricardo Torres, for their hospitality and hard work during the experimental campaign. The authors are also grateful to fellow SINBAD researchers for their feedback on preliminary results and to Suzanne J. M. H. Hulscher for her feedback on the draft manuscript. The useful feedback of two anonymous reviewers is greatly appreciated. The research presented in this paper is part of the SINBAD project, funded by STW (12058) and EPSRC (EP/J00507X/1, EP/J005541/1). We further acknowledge the European Community's FP7 project Hydralab IV (contract no. 261520) for funding the accompanying SandT-Pro experiments and the ACVP development by CNRS-LEGI (D. Hurther, P.-A. Barraud, J.-M. Barnoud). The data supporting the results in the present study will be available upon request (j.vanderzanden@utwente.nl) after the SINBAD project is completed.

References

Battjes, J. A. (1974), Surf similarity, in *Proceedings of the 14th International Conference on Coastal Eng. Copenhagen, Denmark*, pp. 466–480, ASCE, N. Y.

Berni, C., E. Barthélemy, and H. Michallet (2013), Surf zone cross-shore boundary layer velocity asymmetry and skewness: An experimental study on a mobile bed, *J. Geophys. Res. Oceans*, *118*, 2188–2200, doi:10.1002/jgrc.20125.

Boers, M. (2005), Surf zone turbulence, PhD Thesis, TU Delft, Netherlands.

Brinkkemper, J. A., T. Lanckriet, F. Grasso, J. A. Puleo, and B. G. Ruessink (2015), Observations of turbulence within the surf and swash zone of a field-scale sandy laboratory beach, *Coastal Eng.*, *133*, 62–72, doi:10.1016/j.coastaleng.2015.07.006.

Campbell, L. J., T. O'Donoghue, and J. S. Ribberink (2007), Wave Boundary Layer Velocities in Oscillatory Sheet Flow, *Proceedings of the 30th International Conference on Coastal Engineering*, edited by J. M. Smith, pp. 2207–2219, World Scientific, Singapore, San Diego, USA.

Chassagneux, F. X., and D. Hurther (2014), Wave bottom boundary layer processes below irregular surfzone breaking waves with light-weight sheet flow particle transport, *J. Geophys. Res. Oceans*, *119*, 1668–1690, doi:10.1002/2013JC009338.

Christensen, E. D., and R. Deigaard (2001), Large eddy simulation of breaking waves, *Coastal Eng.*, *42*(1), 53–86, doi:10.1016/S0378-3839(00)00049-1.

Cox, D. T., and N. Kobayashi (2000), Identification of intense, intermittent coherent motions under shoaling and breaking waves, *J. Geophys. Res.*, *105*(C6), 14,223–14,236, doi:10.1029/2000JC900048.

Cox, D. T., N. Kobayashi, and A. Okayasu (1996), Bottom shear stress in the surf zone, *J. Geophys. Res.*, *101*(C6), 14,337–14,348, doi:10.1029/96JC00942.

Davies, A. G., R. L. Soulsby, and H. L. King (1988), A numerical-model of the combined wave and current bottom boundary-layer, *J. Geophys. Res.*, *93*(C1), 491–508, doi:10.1029/JC093iC01p00491.

Deigaard, R., J. Fredsøe, and M. B. Mikkelsen (1991), Measurements of the bed shear stress in a surf zone, *Prog. Rep. Inst. Hydodyn. Hydraul. Eng.*, *73*, 21–30.

Dohmen-Janssen, C. M., W. N. Hassan, and J. S. Ribberink (2001), Mobile-bed effects in oscillatory sheet flow, *J. Geophys. Res.*, *106*(C11), 27,103–27,115, doi:10.1029/2000JC000513.

Feddersen, F. (2012). Observations of the surf-zone turbulent dissipation rate, *J. Phys. Oceanogr.*, *42*(3), 386–399, doi:10.1175/Jpo-D-11-082.1.

Feddersen, F., and J.H. Trowbridge (2005), The effect of wave breaking on surf-zone turbulence and alongshore currents: A modeling study, *J. Phys. Oceanogr.*, *35*(11), 2187–2203.

Feddersen, F., and A. J. Williams (2007), Direct estimation of the Reynolds Stress vertical structure in the nearshore, *J. Atmos. Ocean. Technol.*, *24*(1), 102–116, doi:10.1175/jtech1953.1.

Fredsøe, J. (1984), Turbulent boundary layer in wave-current motion, *J. Hydraul. Eng.*, *110*(8), 1103–1120, doi:10.1061/(asce)0733-9429(1984)110:8(1103).

Fredsøe, J., and R. Deigaard (1992), *Mechanics of Coastal Sediment Transport*, World Sci., Singapore.

Fredsøe, J., B. M. Sumer, A. Kozakiewicz, L. H. C. Chua, and R. Deigaard (2003), Effect of externally generated turbulence on wave boundary layer, *Coastal Eng.*, *49*(3), 155–183, doi:10.1016/S0378-3839(03)00032-2.

Fuhrman, D. R., J. Fredsøe, and B. M. Sumer (2009a), Bed slope effects on turbulent wave boundary layers: 1. Model validation and quantification of rough-turbulent results, *J. Geophys. Res.*, *114*, C03024, doi:10.1029/2008JC005045.

Fuhrman, D. R., J. Fredsøe, and B. M. Sumer (2009b), Bed slope effects on turbulent wave boundary layers: 2. Comparison with skewness, asymmetry, and other effects, *J. Geophys. Res.*, *114*, C03025, doi:10.1029/2008JC005053.

Garbini, J. L., F. K. Forster, and J. E. Jorgensen (1982), Measurement of Fluid Turbulence Based on Pulsed Ultrasound Techniques .1. Analysis, *J. Fluid Mech.*, *118*, 445–470, doi:10.1017/S0022112082001153.

Garcez-Faria, A. F., E. B. Thornton, T. C. Lippmann, and T. P. Stanton (2000), Undertow over a barred beach, *J. Geophys. Res.*, *105*(C7), 16,999–17,010, doi:10.1029/2000JC900084.

Govender, K., G. P. Mocke, and M. J. Alport (2002), Video-imaged surf zone wave and roller structures and flow fields, *J. Geophys. Res.*, *107*(C7), doi:10.1029/2000JC000755.

Grasso, F., B. Castelle, and B. G. Ruessink (2012), Turbulence dissipation under breaking waves and bores in a natural surf zone, *Cont. Shelf Res.*, *43*, 133–141, doi:10.1016/j.csr.2012.05.014.

Guza, R. T., and E. B. Thornton (1980), Local and shoaled comparisons of sea surface elevations, pressures, and velocities, *J. Geophys. Res.*, *85*(C3), 1524–1530, doi:10.1029/JC085iC03p01524.

Hsu, T. J., J. T. Jenkins, and P. L. F. Liu (2004), On two-phase sediment transport: Sheet flow of massive particles, *Proc. R. Soc. London Ser. A*, *460*(2048), 2223–2250, doi:10.1098/rspa.2003.1273.

Huang, Z. C., H. H. Hwung, S. C. Hsiao, and K. A. Chang (2010), Laboratory observation of boundary layer flow under spilling breakers in surf zone using particle image velocimetry, *Coastal Eng.*, *57*(3), 343–357, doi:10.1016/j.coastaleng.2009.11.004.

Hurther, D., and U. Lemmin (2001), A correction method for turbulence measurements with a 3D acoustic Doppler velocity profiler, *J. Atmos. Oceanic Technol.*, *18*(3), 446–458, doi:10.1175/1520-0426(2001)018 < 0446:ACMFTM>2.0.CO;2.

Hurther, D., and U. Lemmin (2008), Improved turbulence profiling with field-adapted acoustic doppler velocimeters using a bifrequency doppler noise suppression method, *J. Atmos. Oceanic Technol.*, *25*(3), 452–463, doi:10.1175/2007JTECHO512.1.

Hurther, D., and P. D. Thorne (2011), Suspension and near-bed load sediment transport processes above a migrating, sand-rippled bed under shoaling waves, *J. Geophys. Res.*, *116*, C07001, doi:10.1029/2010JC006774.

Hurther, D., P. D. Thorne, M. Bricault, U. Lemmin, and J. M. Barnoud (2011), A multi-frequency Acoustic Concentration and Velocity Profiler (ACVP) for boundary layer measurements of fine-scale flow and sediment transport processes, *Coastal Eng.*, *58*(7), 594–605, doi:10.1016/j.coastaleng.2011.01.006.

Jacobsen, N. G., J. Fredsøe, and J. H. Jensen (2014), Formation and development of a breaker bar under regular waves. Part 1: Model description and hydrodynamics, *Coastal Eng.*, *88*, 182–193, doi:10.1016/j.coastaleng.2013.12.008.

Jensen, B. L., B. M. Sumer, and J. Fredsøe (1989), Turbulent Oscillatory boundary-layers at high Reynolds-numbers, *J. Fluid Mech.*, *206*, 265–297, doi:10.1017/S0022112089002302.

Kemp, P. H., and R. R. Simons (1983), The interaction of waves and a turbulent current: Waves propagating against the current, *J. Fluid Mech.*, *130*, 73–89, doi:10.1017/S0022112083000981.
Kimmoun, O., and H. Branger (2007), A particle image velocimetry investigation on laboratory surf-zone breaking waves over a sloping beach, *J. Fluid Mech.*, *588*, 353–397, doi:10.1017/S0022112007007641.
Kranenburg, W. M., J. S. Ribberink, R. E. Uittenbogaard, and S. J. M. H. Hulscher (2012), Net currents in the wave bottom boundary layer: On waveshape streaming and progressive wave streaming, *J. Geophys. Res.*, *117*, F03005, doi:10.1029/2011JF002070.
Melville, W. K., F. Veron, and C. J. White (2002), The velocity field under breaking waves: Coherent structures and turbulence, *J. Fluid Mech.*, *454*, 203–233, doi:10.1017/S0022112001007078.
Naqshband, S., J. S. Ribberink, D. Hurther, and S. J. M. H. Hulscher (2014), Bed load and suspended load contributions to migrating sand dunes in equilibrium, *J. Geophys. Res. Earth Surf.*, *119*, 1043–1063, doi:10.1002/2013JF003043.
Nielsen, P. (1992), *Coastal Bottom Boundary Layers and Sediment Transport*,World Sci., Singapore.
O'Donoghue, T., and S. Wright (2004), Flow tunnel measurements of velocities and sand flux in oscillatory sheet flow for well-sorted and graded sands, *Coastal Eng.*, *51*(11–12), 1163–1184, doi:10.1016/j.coastaleng.2004.08.001.
Peregrine, D. H. (1983), Breaking waves on beaches, *Annu. Rev. Fluid Mech.*, *15*(1), 149–178, doi:10.1146/annurev.fl.15.010183.001053.
Revil-Baudard, T., J. Chauchat, D. Hurther, and P.-A. Barraud (2015), Investigation of sheet-flow processes based on novel acoustic high-resolution velocity and concentration measurements, *J. Fluid Mech.*, *767*, 1–30, doi:10.1017/jfm.2015.23.
Ribberink, J. S., D. A. Van der A, J. Van der Zanden, T. O'Donoghue, D. Hurther, I. Cáceres, and P. D. Thorne (2014), SandT-Pro: Sediment transport measurements under irregular and breaking waves, In *Proceedings of the 34th International Conference on Coastal Engineering*, 14 pp., Coastal Engineering Research Council, Seoul, Korea.
Ruessink, B. G. (2010), Observations of turbulence within a natural surf zone, *J. Phys. Oceanogr.*, *40*(12), 2696–2712, doi:10.1175/2010JPO4466.1.
Ruessink, B. G., H. Michallet, T. Abreu, F. Sancho, D. A. Van der A, J. J. Van der Werf, and P. A. Silva (2011), Observations of velocities, sand concentrations, and fluxes under velocity-asymmetric oscillatory flows, *J. Geophys. Res.*, *116*, C03004, doi:10.1029/2010JC006443.
Schretlen, J. L. M. (2012), Sand transport under full-scale progressive surface waves, PhD thesis, Univ. of Twente, Netherlands.
Scott, C. P., D. T. Cox, T. B. Maddux, and J. W. Long (2005), Large-scale laboratory observations of turbulence on a fixed barred beach, *Meas. Sci. Technol.*, *16*(10), 1903–1912, doi:10.1088/0957-0233/19/10/004.
Sleath, J. F. A. (1991), Velocities and shear stresses in wave-current flows, *J. Geophys. Res.*, *96*(C8), 15,237–15,244, doi:10.1029/91JC01458.
Smith, E. R., and N. C. Kraus (1991), Laboratory study of wave-breaking over bars and artificial reefs, *J. Waterw. Port Coastal Ocean Eng.*, *117*(4), 307–325, doi:10.1061/(ASCE)0733-950X(1991)117:4(307).
Soulsby, R. L. (1980), Selecting Record Length and Digitization Rate for Near-Bed Turbulence Measurements, *J. Phys. Oceanogr.*, *10*(2), 208–219, doi:10.1175/1520-0485(1980)010<0208:srladr>2.0.co;2.
Sumer, B. M., and B. Oguz (1978), Particle motions near bottom in turbulent-flow in an open channel, *J. Fluid Mech.*, *86*, 109–127, doi:10.1017/S0022112078001020.
Sumer, B. M., T. S. Laursen, and J. Fredsøe (1993), Wave boundary layers in a convergent tunnel, *Coastal Eng.*, *20*(3-4), 317–342, doi:10.1016/0378-3839(93)90006-t.
Sumer, B. M., A. Kozakiewicz, J. Fredsøe, and R. Deigaard (1996), Velocity and concentration profiles in sheet-flow layer of movable bed, *J. Hydraul. Eng.*, *122*(10), 549–558, doi:10.1061/(ASCE)0733-9429(1996)122:10(549).
Sumer, B. M., L. H. C. Chua, N. S. Cheng, and J. Fredsøe (2003), Influence of turbulence on bed load sediment transport, *J. Hydraul. Eng.*, *129*(8), 585–596, doi:10.1061/(ASCE)0733-9429(2003)129:8(585).
Sumer, B. M., H. A. A. Guner, N. M. Hansen, D. R. Fuhrman, and J. Fredsøe (2013), Laboratory observations of flow and sediment transport induced by plunging regular waves, *J. Geophys. Res. Oceans*, *118*, 6161–6182, doi:10.1002/2013JC009324.
Svendsen, I. A. (1987), Analysis of surf zone turbulence, *J. Geophys. Res.*, *92*(C5), 5115–5124, doi:10.1029/JC092iC05p05115.
Svendsen, I. A., P. A. Madsen, and J. Buhr Hansen (1978), Wave characteristics in the surf zone, in *Proceedings of the 16th Conference Coastal Engineering*, pp. 520–539, American Society of Civil Engineers, N. Y.
Thornton, E. B., and R. T. Guza (1983), Transformation of wave height distribution, *J. Geophys. Res.*, *88*(C10), 5925–5938, doi:10.1029/JC088iC10p05925.
Ting, F. C. K., and J. T. Kirby (1994), Observation of undertow and turbulence in a laboratory surf zone, *Coastal Eng.*, *24*(1–2), 51–80, doi:10.1016/0378-3839(94)90026-4.
Ting, F. C. K., and J. T. Kirby (1995), Dynamics of surf-zone turbulence in a strong plunging breaker, *Coastal Eng.*, *24*(3–4), 177–204, doi:10.1016/0378-3839(94)00036-W.
Ting, F. C. K., and J. R. Nelson (2011), Laboratory measurements of large-scale near-bed turbulent flow structures under spilling regular waves, *Coastal Eng.*, *58*(2), 151–172, doi:10.1016/j.coastaleng.2010.09.004.
Trowbridge, J., and O. S. Madsen (1984), Turbulent wave boundary-layers .2. 2nd-order theory and mass-transport, *J. Geophys. Res.*, *89*(C5), 7999–8007.
van der A, D. A., T. O'Donoghue, A. G. Davies, and J. S. Ribberink (2011), Experimental study of the turbulent boundary layer in acceleration-skewed oscillatory flow, *J. Fluid Mech.*, *684*, 251–283, doi:10.1017/jfm.2011.300.
van der A, D. A., J. S. Ribberink, J. J. van der Werf, T. O'Donoghue, R. H. Buijsrogge and W. M. Kranenburg (2013), Practical sand transport formula for non-breaking waves and currents, *Coastal Eng.*, *76*, 26–42, doi:10.1016/j.coastaleng.2013.01.007.
van Doorn, T. (1981). Experimental investigation of near-bottom velocities in water waves without and with a current, *TOW Rep. M 1423*, Part 1, Delft Hydraul. Lab., Delft, Netherlands.
van Rijn, L. C. (2007). Unified view of sediment transport by currents and waves. I: Initiation of motion, bed roughness, and bed-load transport, *J. Hydraul. Eng.*, *133*(6), 649–667, doi:10.1061/(ASCE)0733-9429(2007)133:6(649).
Yoon, H. D., and D. T. Cox (2010), Large-scale laboratory observations of wave breaking turbulence over an evolving beach, *J. Geophys. Res.*, *115*, C10007, doi:10.1029/2009JC005748.